CrystEngComm

PAPER

View Article Online
View Journal | View Issue

Cite this: *CrystEngComm*, 2024, **26**, 3609

NIR-enhanced multi-mode catalytic activity over Pd nanocrystals sandwiched within magnetic polydopamine hollow spheres†

Jie Jin,*[a] Haoran Li,[a] Shanshan Wu,[a] Jing Wang,[b] Qunling Fang,[b] Chunyan Xu,*[c] Yunqi Xu,[d] Weili Kong,[a] Di Wang[a] and Shouhu Xuan*[d]

Received 15th May 2024,
Accepted 27th May 2024

DOI: 10.1039/d4ce00490f

rsc.li/crystengcomm

With the rapid development of social industrialization, energy crisis and environmental problems are becoming increasingly serious. Therefore, there is an urgent need to synthesize multi-mode nanocatalysts for general application. In this paper, a h-Fe_3O_4@Pd/PDA nanocatalyst with Pd nanocrystals sandwiched between a h-Fe_3O_4 hollow sphere and a polydopamine (PDA) shell was prepared by a simple redox-oxidative polymerization method. The catalytic activity of h-Fe_3O_4@Pd/PDA hollow spheres was evaluated using selective reduction hydrogenation of 4-nitrostyrene, reduction of 4-nitrophenol and oxidation of 3,3′,5,5′-tetramethylbenzidine (TMB) as catalytic models. h-Fe_3O_4@Pd/PDA has reduction kinetics of 4-nitrophenol up to 0.77 min^{-1} mg^{-1}. Importantly, the rate of 4-nitrophenol reduction catalyzed by h-Fe_3O_4@Pd/PDA was enhanced by 1.43 times under near infrared light (NIR, 808 nm) irradiation. In addition, NIR laser can induce the selective reduction of 4-nitrostyrene to 4-aminostyrene by h-Fe_3O_4@Pd/PDA with a selectivity of 84.8%. Under different reaction scenarios, h-Fe_3O_4@Pd/PDA hollow spheres could be recycled by magnetic recovery, and the catalytic reaction activity was above 70% after six cycles. As a result, owing to the simple fabrication, good magnetic separation and high NIR-enhanced catalytic properties, h-Fe_3O_4@Pd/PDA exhibited a wide range of potential in nanocatalysis.

1. Introduction

Due to their high catalytic activity, noble metal nanocrystals possess great potential in nanocatalysis such as hydrogenation of nitroaromatic hydrocarbons, catalytic degradation of heavy metal ions, catalytic Suzuki–Miyaura coupling and Heck reaction.[1–4] Among them, Pd nanocatalysts have received considerable attention in the field of heterogeneous catalysis. During the past decade, various methods such as controlling high temperature conditions, inert gas protection, long reaction time and complex reaction steps have been developed to synthesize high-quality Pd nanocrystals for improving their catalytic activity.[5–10] It was found that the catalytic performance of Pd nanocrystals could be modulated by varying the experimental strategies.[11,12] However, the high surface energy of Pd nanocrystals often led them to be easily aggregated, resulting in low stability and irregular morphology, which limited their practical application. Therefore, the optimization of structural stability is considered to be an important factor to improve the catalytic performance of Pd nanocrystals.[13–15]

Multifunctional nanoplatforms received increasing research interest in carrying nanocatalysts since they could maintain good dispersion, prevent the leaching of nanocatalysts, and endow them with easy separation characteristics.[16,17] To improve the stability and efficiency of Pd nanocatalysts, a large number of nanocarriers, such as SiO_2,[18] metal–organic frameworks,[19] metal oxides,[20,21] polymers,[22] and Fe_3O_4,[23–28] have been applied for catalytically active metals. These non-toxic, easy to recover, and cost-effective nanoplatforms guaranteed high efficiency for heterogeneous catalysis. However, due to the weak interaction between the nanocarrier and active metals, it is still a challenge to protect the nanocatalysts from leaching during the recycling catalytic reactions even if surface modification has been introduced to enhance interaction.[29,30] As a result, coating another layer on the nanoplatforms which have already been immobilized by the nanocatalysts becomes one possible solution. Previously, various immobilized

[a] School of Materials and Chemical Engineering, Anhui Jianzhu University, Hefei, 230601, PR China. E-mail: jinjie@ahjzu.edu.cn
[b] School of Food and Biological Engineering, Hefei University of Technology, Hefei, 230009, PR China
[c] School of Resources and Environmental Engineering, Anhui University, Hefei, 230601, PR China. E-mail: Chunyan.xu@ahu.edu.cn
[d] CAS Key Laboratory of Mechanical Behavior and Design of Materials, Department of Modern Mechanics, University of Science and Technology of China, Hefei, 230026, PR China. E-mail: xuansh@ustc.edu.cn

† Electronic supplementary information (ESI) available. See DOI: https://doi.org/10.1039/d4ce00490f

nanocatalysts with sandwich-like nanostructure have been intensively investigated. However, the mostly reported layer-by-layer preparation was complicated which significantly limited its practicality.[31,32]

The one-step encapsulation method is attractive in carrying nanocatalysts due to its high economic efficiency. During the past decades, various methods have been proposed for easy preparation of polymer-encapsulated noble metal nanocatalysts. Ye *et al.* used a one-step reduction method to synthesize polydopamine (PDA) wrapping Ag/graphene hybrids for efficient oxidation of hydroquinone to benzoquinone.[33] Bai *et al.* reported a novel sandwich-structured magnetic microsphere (Fe_3O_4@RF-Pt@PDA) that can efficiently catalyze the oxidation of 3,3′,5,5′-tetramethylbenzidine (TMB).[34] PDA, an interesting mesoporous polymer which usually exhibits strong adhesion on various substrates *via* strong intermolecular interactions, has been intensively applied to protect noble metal nanocrystals from leaching.[35,36] It was reported that Au could be simultaneously covered by the PDA layer *via* a one-step redox-polymerization method.[35] Because of the easy preparation and uniform coating, this strategy is attractive in guaranteeing the stability of the nanocatalyst. However, due to the weak formation dynamics, it is still very difficult to *in situ* encapsulate the Pd nanocrystals within PDA.

Noble metal nanocrystals possess the physical properties of localized surface plasmon resonance (LSPR), which can effectively enhance spectral absorption and generate hot electrons and photothermal effects.[37–39] Moreover, it has been discovered that the catalytic rate of nanocatalysts increased when exposed to NIR photothermal conditions. Under the PDA layer coating, the photothermal effect would be increased.[40] As a result, improved catalytic dynamics have been distinctively observed in many noble metal–PDA hybrid nanocomposites. However, the multi-mode NIR-enhanced catalytic mechanism in various reaction systems has not been intensively discussed. Moreover, the reuse of nanocatalysts is also an enormous problem in chemical production. Compared with traditional recovery methods, magnetic absorption is undoubtedly a novel and simple recovery method. In consideration of the important application of Pd nanocatalysts, the development of magnetically separable Pd nanocatalysts with NIR-enhanced catalytic activity and investigation of their multi-mode catalytic mechanism becomes an urgent requirement.

This work reports a simple redox-oxidative polymerization method to synthesize h-Fe_3O_4@Pd/PDA hollow spheres, which possess excellent photothermal characteristics, high catalytic activities, and good superparamagnetic behavior. Due to the presence of inner Pd nanocrystals, the h-Fe_3O_4@Pd/PDA hollow spheres show a multi-mode catalytic activity. Originating from the remarkable plasmon resonance (LSPR) and photothermal property, the catalytic reaction rates on reducing 4-nitrostyrene and 4-nitrophenol, and oxidation of TMB can be significantly enhanced under NIR light irradiation. The superparamagnetism and the PDA coating layer in h-Fe_3O_4@Pd/PDA hollow spheres ensure both magnetic recyclability and cyclic catalytic activity, thereby providing a wide range of potential applications in nanocatalysis.

2. Experimental section

2.1. Materials

Iron(III) chloride hexahydrate ($FeCl_3{\cdot}6H_2O$), polyacrylamide (PAM), sodium citrate ($C_6H_5Na_3O_7{\cdot}2H_2O$), ethanol (EtOH), urea (H_2NCONH_2), palladium(II) chloride ($PdCl_2$), (3-aminopropyl) triethoxysilane (APTES, $C_9H_{23}NO_3Si$), sodium borohydride ($NaBH_4$), 3-hydroxytyrosine hydrochloride (DA-HCl), trihydroxymethyl aminomethane (Tris-HCl), sodium acetate ($C_2H_3NaO_2$), glacial acetic acid ($C_2H_4O_2$) and 4-nitrophenol ($C_6H_5NO_3$) were purchased from Sinopharm Chemical Reagent Co., Ltd. 3,3′,5,5′-Tetramethylbenzidine (TMB), hydrogen peroxide (H_2O_2), 4-nitrostyrene ($C_8H_7NO_2$) and borane–ammonia complex (NH_3BH_3) were purchased from Aladdin Chemical Co., Ltd, China. All reagents were used as received without further purification and ultrapure water was used in all experiments.

2.2. Preparation of h-Fe_3O_4@Pd/PDA hollow spheres

Preparation of h-Fe_3O_4 hollow spheres. h-Fe_3O_4 hollow spheres were synthesized by solvothermal reaction.[41] First, $FeCl_3{\cdot}6H_2O$ (0.54 g), urea (0.36 g), sodium citrate (1.2 g) and PAM (0.3 g) were dissolved in 40 mL of deionized water. After complete dissolution, the homogeneous mixture was transferred to a Teflon-lined stainless-steel autoclave and heated at 200 °C for 12 h. After cooling to room temperature, the h-Fe_3O_4 hollow spheres were alternately washed with deionized water and ethanol several times. Finally, h-Fe_3O_4 hollow spheres were obtained after vacuum drying at 40 °C.

Preparation of h-Fe_3O_4@Pd/PDA hollow spheres. Monodisperse h-Fe_3O_4@Pd/PDA hollow spheres were prepared by a simple redox-oxidative polymerization method. First, 18 mg h-Fe_3O_4 hollow spheres were ultrasonically dispersed in 50 mL ethanol. Then, APTES solution (200 μL) was added. After 2 h, the obtained h-Fe_3O_4-APTES spheres were washed alternately with ethanol and water, and then they were ultrasonically dispersed in 50 mL ethanol, followed by adding $NaBH_4$ (10 mg), sodium citrate (20 mg), H_2PdCl_4 (0.01 M, 8.8 mL), DA-HCl (25 mg), and 25 mL of Tris-HCl (pH 8.5). After 4 h, the product was collected from the solution with a magnet and alternately washed with deionized water and ethanol. Finally, the product was obtained after vacuum drying.

The second preparation method of h-Fe_3O_4@Pd/PDA hollow spheres. First, 15 mg h-Fe_3O_4 hollow spheres were ultrasonically dispersed in 50 mL ethanol, followed by the addition of PVP (0.1 g) and ultrasonication for 1 h. Then, magnetic stirring was performed. After 14 h, the reaction system was transferred to ultrasonication. After 30 min, $NaBH_4$ (10 mg) and H_2PdCl_4 (0.01 M, 8.8 mL) were added. At intervals of 30 min, Tris-HCl buffer mixed with dopamine (25

mg) was poured into the conical flask. After 4 h, the product was collected with a magnet and washed alternately with deionized water and ethanol. Finally, the product was obtained by vacuum drying.

Preparation of h-Fe_3O_4/PDA, h-Fe_3O_4@Au/PDA, and h-Fe_3O_4@Ag/PDA hollow spheres. h-Fe_3O_4@PDA, h-Fe_3O_4@Au/PDA, and h-Fe_3O_4@Ag/PDA were synthesized in a similar manner to that of h-Fe_3O_4@Pd/PDA. Among them, $HAuCl_4$ (100 μL, 0.24 M) was added to the synthesis of h-Fe_3O_4@Au/PDA. $Ag(NH_3)_2OH$ (0.5 mL, 8.8×10^{-5} M) was added to the synthesis of h-Fe_3O_4@Ag/PDA.

Preparation of MXene@Pd/PDA nanosheets, SiO_2@Pd/PDA nanospheres and α-Fe_2O_3@Pd/PDA nanoellipsoids. Firstly, MXene nanosheets, SiO_2 nanospheres, α-Fe_2O_3 nanoellipsoids were synthesized using a method from the literature.[42–44] The subsequent synthesis methods were consistent with that of h-Fe_3O_4@Pd/PDA hollow spheres.

2.3. Photothermal properties of h-Fe_3O_4@Pd/PDA hollow spheres

First, the absorbance of h-Fe_3O_4@Pd/PDA suspensions of different concentrations (20, 40, 60, 80 and 100 μg mL^{-1}) at 808 nm was determined. Secondly, 1 mL of h-Fe_3O_4@Pd/PDA with different concentrations was added into a 1.5 mL centrifuge tube, and the temperature changes during heating and cooling of the nanocomposites under NIR light (808 nm, 2.0 W cm^{-2}) were recorded by an infrared camera every 15 s for 6 min. The photothermal property was calculated and analyzed. The photothermal conversion efficiency, heating and cooling conditions and circulating heating effect of h-Fe_3O_4@Pd/PDA were analyzed.

2.4. Catalytic properties of h-Fe_3O_4@Pd/PDA hollow spheres

Catalytic activity of h-Fe_3O_4@Pd/PDA hollow spheres on selective reductive hydrogenation of 4-nitrostyrene. Firstly, 15 mg 4-nitrostyrene, 8 mg h-Fe_3O_4@Pd/PDA hollow spheres, 20 mg NH_3BH_3 and 5 mL ethanol were added to the reaction flask. Then, the reaction was performed under NIR light (808 nm, 2.0 W cm^{-2}). The conversion of 4-nitrostyrene was monitored with a UV-vis spectrophotometer every 5 or 10 min until the reaction was completed. After the reaction, the experimental results were accurately detected by GC-MS spectrometry. For catalytic cycle experiments, h-Fe_3O_4@Pd/PDA was separated by a strong magnet after reaction, washed with water and ethanol twice, and then recycled.

Catalytic activity of h-Fe_3O_4@Pd/PDA hollow spheres on reducing 4-nitrophenol. Firstly, h-Fe_3O_4@Pd/PDA hollow spheres (3 mg) and $NaBH_4$ (70 mg) were dispersed in 4-nitrophenol aqueous solution (1×10^{-4} M, 50 mL). During the reaction, the color of the mixed solution changed from yellow to colorless. In order to monitor the transformation of 4-nitrophenol, a UV-vis spectrophotometer was used to detect it every 15 s or 30 s until the reaction was completed. Finally, the h-Fe_3O_4@Pd/PDA hollow spheres were separated from the reaction system by a magnet and reused for subsequent cycle experiments. The apparent first-order rate constant k_a of 4-nitrophenol was determined by tracking the change of absorbance at 400 nm with time to determine the catalytic activity of the catalyst. Excess $NaBH_4$ ensures the pseudo-first-order kinetics of the reaction.

The rate constant (k_a) was determined according to the following equation:

$$\ln\left(\frac{A_t}{A_0}\right) = \ln\left(\frac{C_t}{C_0}\right) = -k_a t \tag{1}$$

where A_0 and A_t are the absorbance intensities of the characteristic peaks at the initial and reaction time t of 4-nitrophenol solution, respectively. C_0 and C_t are the solution concentrations at the initial and reaction time t, respectively.

In order to compare the catalytic performance of h-Fe_3O_4@Pd/PDA with other reported catalysts for 4-nitrophenol, the normalized ratio constant was calculated as follows:

$$k_n = \frac{k_a}{m} \tag{2}$$

where m (mg) is the mass of the catalyst.

Catalytic activity of h-Fe_3O_4@Pd/PDA hollow spheres on TMB. The reaction bottle containing h-Fe_3O_4@Pd/PDA (20 μg mL^{-1}), TMB (0.2 mM), H_2O_2 (0.5 mM) and HAc-NaAc buffer aqueous solution (pH 3) was placed in a 60 °C water bath for 10 min. After the reaction, the absorbance value at 652 nm was measured. In this experiment, all experimental data were measured three times. In order to compare the effect of pH on the relative activity of h-Fe_3O_4@Pd/PDA, the catalytic reaction of h-Fe_3O_4@Pd/PDA at pH 2–12 of HAc–NaAc buffer at 60 °C was investigated. To study the effect of temperature on the relative activity of h-Fe_3O_4@Pd/PDA, the catalytic reaction was carried out in a water bath of 30–80 °C at pH 3. In addition, the cyclic activity of h-Fe_3O_4@Pd/PDA in the standard reaction system was studied by a magnetic separation method. The enzyme activities of h-Fe_3O_4, h-Fe_3O_4/PDA, and h-Fe_3O_4@Pd/PDA hollow spheres were investigated by the above standard reaction methods. Then, the catalytic activity of h-Fe_3O_4@Pd/PDA under different heating conditions was investigated.

In the steady-state dynamic tests, the concentration of TMB (0.2–1.6 mM) or H_2O_2 (0.2–1.6 mM) was changed to perform the experiment while other conditions remained unchanged.

The kinetic parameters K_m and V_{max} were calculated according to the Lineweaver–Burk diagram, which was the double reciprocal diagram of the Michaelis–Menten equation:

$$\frac{1}{v_0} = \left(\frac{K_m}{V_{max}}\right)\left(\frac{1}{[S]}\right) + \frac{1}{V_{max}} \tag{3}$$

where v_0 is the initial velocity, V_{max} is the maximum reaction velocity, [S] is the substrate concentration, and K_m is the Michaelis–Menten constant.

2.5. Characterization

Field emission transmission electron microscopy (FE-TEM, JEM-2100F) was used to observe the morphology and nanostructure of the samples. The crystal structure of the samples was determined by X-ray diffraction (XRD, SmartLab). X-ray photoelectron spectrometry (XPS, ESCALAB250Xi) was used to determine the surface elements and the chemical states of materials. The functional groups of all samples in the range of 4000–500 cm^{-1} wavenumber were analyzed by FTIR (TENSOR27). An inductively coupled plasma-mass spectrometer (ICP-AES, iCAP 7400) was used to analyze the metal content in the products. A UV spectrophotometer (UV-1800, Shimadzu) was used to determine the absorbance of the substances during the catalytic process. Gas Chromatography Q Exactive Orbitrap Mass Sepctrometer (GC-MS, Q Exactive GC) was used to separate and identify the complex components.

3. Results and discussion

3.1. Synthesis and characterization of h-Fe_3O_4@Pd/PDA hollow spheres

Fig. 1a shows the synthesis diagram of h-Fe_3O_4@Pd/PDA hollow spheres. First, h-Fe_3O_4 hollow spheres were synthesized by solvothermal reaction according to a previous report.[41] Then, the h-Fe_3O_4 hollow spheres were dispersed in ethanol and modified by APTES. H_2PdCl_4, $NaBH_4$, and DA-HCl were mixed with Tris buffer solution suspended with APTES-modified h-Fe_3O_4 hollow spheres. After 4 h, the h-Fe_3O_4@Pd/PDA hollow spheres were obtained. Transmission electron microscopy (TEM) images (Fig. 1b and e) show that the h-Fe_3O_4 hollow spheres are relatively uniform in size and have good dispersion. The sample exhibits an obvious hollow nanostructure and the average size is about 284 nm (Fig. S1a†). If dopamine was added into the suspension, h-Fe_3O_4/PDA hollow spheres could be successfully obtained due to

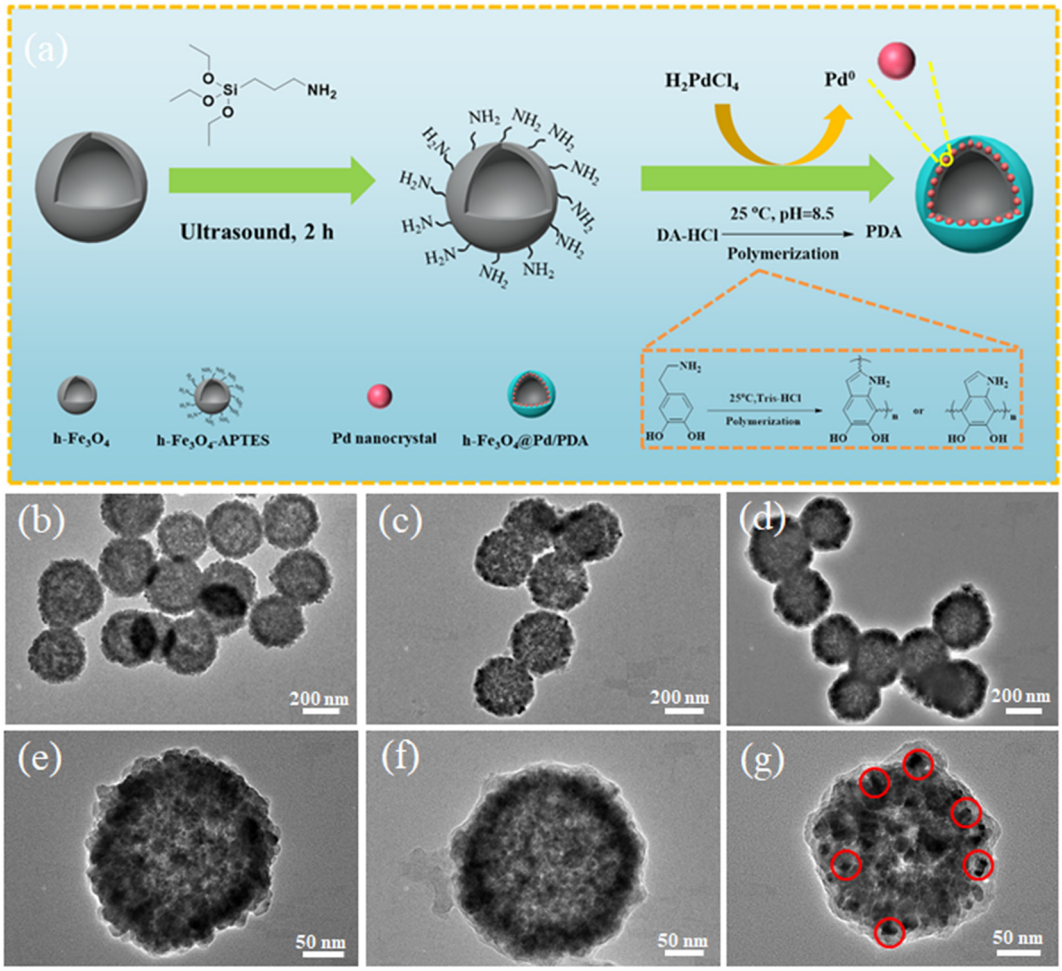

Fig. 1 Schematic diagram of the synthesis process of h-Fe_3O_4@Pd/PDA (a). TEM images of h-Fe_3O_4 (b and e), h-Fe_3O_4/PDA (c and f) and h-Fe_3O_4@Pd/PDA (d and g); red circles mark Pd nanocrystals.

the facile polymerization of the dopamine to form polydopamine. Fig. 1c and f are TEM images of h-Fe_3O_4/PDA hollow spheres, and it can be seen that the outer gray and white area is the PDA layer. The average size is about 305 nm, which is critically larger than that of the pristine h-Fe_3O_4 (Fig. S1b†). When H_2PdCl_4 was introduced into the reaction, h-Fe_3O_4@Pd/PDA hollow spheres were obtained (Fig. 1d and g). Clearly, the h-Fe_3O_4@Pd/PDA hollow spheres have a three-layer nanostructure. The average size of the h-Fe_3O_4@Pd/PDA hollow spheres is about 320 nm (Fig. S1c†). Between the continuous inner hollow Fe_3O_4 core and the outer gray PDA layer, there is a layer of small and non-continuously dispersed Pd nanocrystals. The content of Pd nanocrystals determined by ICP-AES was 19.3 wt% (Table S1†). The above results indicate that the Pd nanocrystals can be facilely carried by the h-Fe_3O_4/PDA hybrid nanocomposites. Different from previous reports,[45,46] the Pd nanocrystals are sandwiched between the h-Fe_3O_4 and the PDA layer, which ensures good protection of the nanocatalysts.

The nanostructure of h-Fe_3O_4@Pd/PDA hollow spheres was further studied by using high-angle annular dark field scanning electron microscopy (HAADF-STEM) and energy-dispersive X-ray (EDX) spectroscopy elemental maps (Fig. 2). Obviously, the core–shell nanostructure of the h-Fe_3O_4@Pd/PDA hollow sphere is mainly composed of Fe, C, O, N and Pd (Fig. 2b–f), in which Fe and O elements are derived from Fe_3O_4 while C and N elements belong to PDA. The distribution diameter of Pd elements (Fig. 2f) is larger than that of Fe and O elements (Fig. 2b and d) and smaller than that of C and N elements (Fig. 2c and e), indicating that Pd nanocrystals are sandwiched between the h-Fe_3O_4 core and the PDA layer, which is also consistent with TEM images. Here, the distribution of the Pd element is not uniform and this result must be originating from the quick formation dynamics during the $NaBH_4$ reduction. In conclusion, the Pd nanocrystals can be easily immobilized on the h-Fe_3O_4 hollow spheres and they are also *in situ* encapsulated within the PDA layer to acquire a sandwich-like nanostructure.

The XRD patterns of h-Fe_3O_4, h-Fe_3O_4/PDA and h-Fe_3O_4@Pd/PDA hollow spheres are measured to analyze the crystallization (Fig. 3a). h-Fe_3O_4 hollow spheres show a typical face-centered cubic phase (JCPDS Card No. 19-0629). Since the nanospheres are composed of secondary nanoparticles, the diffraction peaks are relatively broad. All of the h-Fe_3O_4, h-Fe_3O_4/PDA and h-Fe_3O_4@Pd/PDA have similar Fe_3O_4 diffraction peaks, indicating that the crystal structure of h-Fe_3O_4 has not been affected by Pd/PDA loading. Differently, the intensity of Fe_3O_4 diffraction peaks was slightly decreased after the PDA coating, which indicated the successful coating of the PDA layer on h-Fe_3O_4 hollow spheres. For h-Fe_3O_4@Pd/PDA, the peaks at 2θ of 40.2°, 46.64° and 68.2° correspond to the (111), (200), and (220) crystal planes of pure Pd phase with fcc structure (JCPDS Card No. 46-1043). The above result directly demonstrates that the Pd nanocrystals have been well immobilized on the h-Fe_3O_4@Pd/PDA.

Due to the poor crystallinity of the PDA layer, it cannot be detected by XRD. Therefore, the composition of h-Fe_3O_4@Pd/PDA hollow spheres was further investigated by thermogravimetric analysis (TGA). The weight losses of h-Fe_3O_4, h-Fe_3O_4/PDA, and h-Fe_3O_4@Pd/PDA hollow spheres are 3.84 wt%, 7.41 wt% and 20.5 wt%, respectively (Fig. 3b). The weight loss of h-Fe_3O_4 may be due to absorbed H_2O and

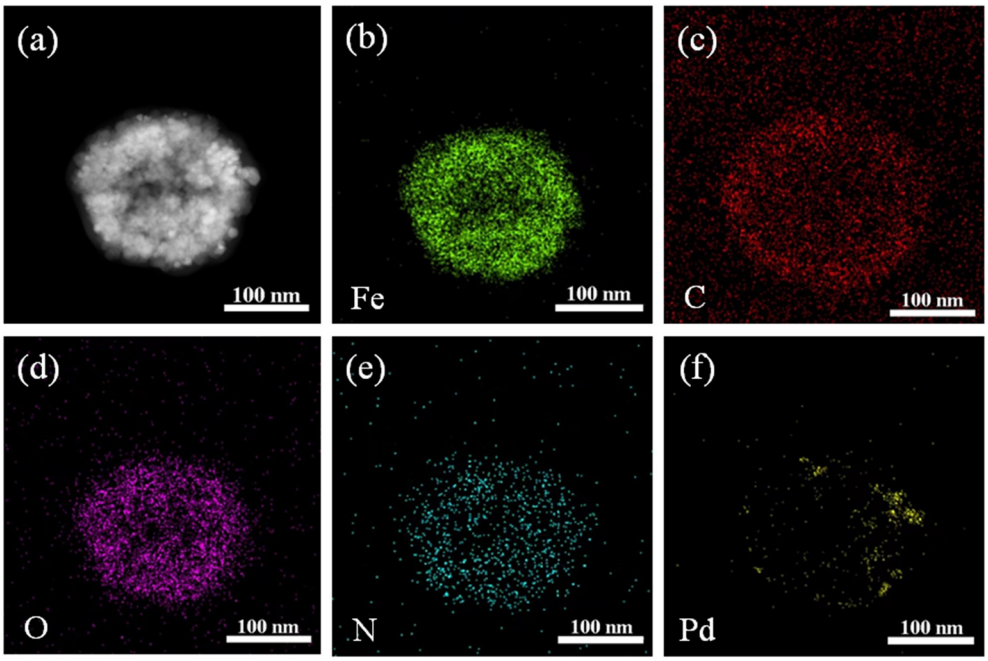

Fig. 2 HAADF-STEM image (a). EDX elemental mapping of Fe, C, O, N and Pd of h-Fe_3O_4@Pd/PDA hollow spheres (b–f).

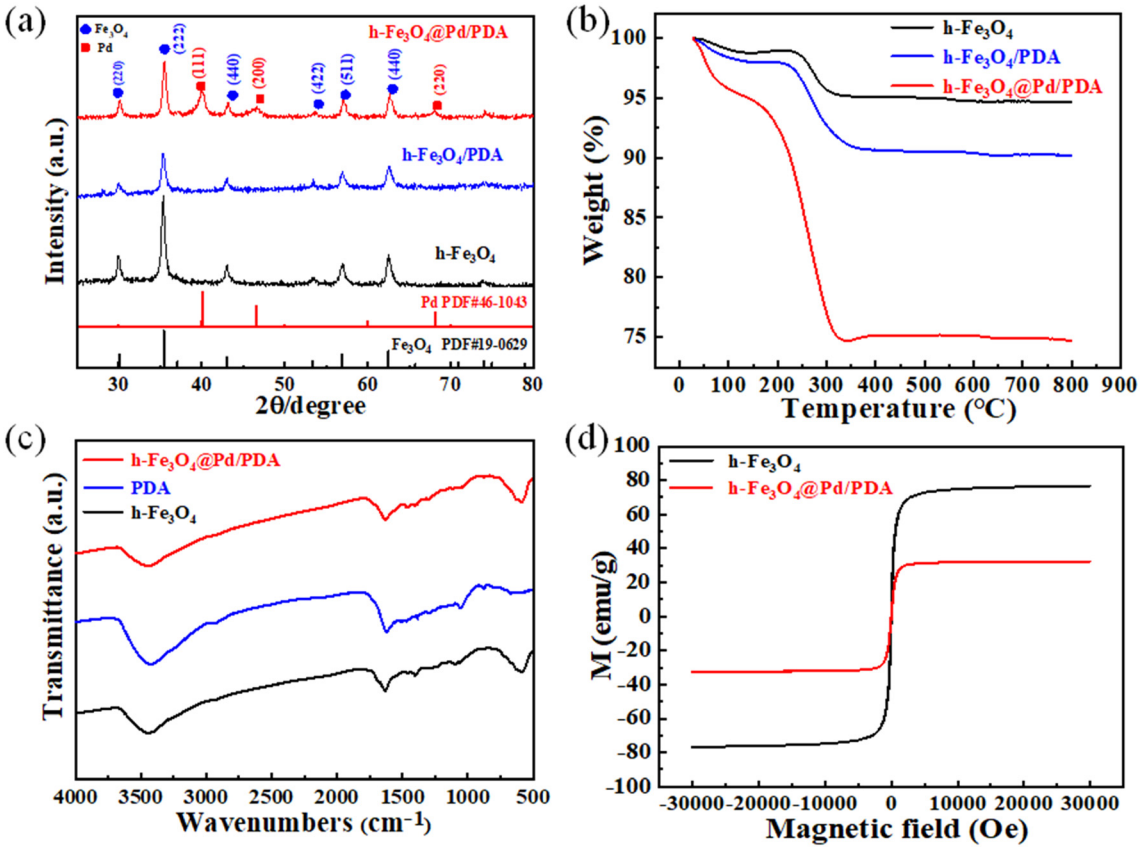

Fig. 3 XRD diffraction patterns (a) and TG curves of h-Fe_3O_4, h-Fe_3O_4/PDA, and h-Fe_3O_4@Pd/PDA (b). FTIR spectra of h-Fe_3O_4, PDA, and h-Fe_3O_4@Pd/PDA (c). Magnetization hysteresis loops of h-Fe_3O_4 and h-Fe_3O_4@Pd/PDA (d).

residual functional groups. Due to the decomposition of the PDA shell, the weight loss of h-Fe_3O_4/PDA is increased compared to that of h-Fe_3O_4. Finally, the noble metal nanocrystals are conducive to promoting the polymerization of PDA, resulting in h-Fe_3O_4@Pd/PDA having the highest weight loss rate.[47] Finally, the largest weight loss is obtained in h-Fe_3O_4@Pd/PDA. Fig. 3c shows the FTIR spectra of h-Fe_3O_4, PDA, and h-Fe_3O_4@Pd/PDA in the range of 4000–500 cm^{-1}. A typical peak of h-Fe_3O_4 at 580 cm^{-1} indicates the presence of Fe–O. The absorption peaks at 3430 and 1630 cm^{-1} are attributed to the amide structure of residual PAM during the synthesis of h-Fe_3O_4. After coating the Pd/PDA layer, the absorption intensities between 800 and 1700 cm^{-1} are increased. Here, the peaks at 3440 and 1620 cm^{-1} must be attributed to the amide structure of residual PAM or the stretching vibration of –OH/–NH_2 or C═O of PDA.

Originating from h-Fe_3O_4, the h-Fe_3O_4@Pd/PDA hollow spheres show typical magnetic characteristics. The hysteresis loops of h-Fe_3O_4 and h-Fe_3O_4@Pd/PDA hollow spheres were measured by VSM at room temperature. It can be seen from the magnetization curve (Fig. 3d) that both h-Fe_3O_4 and h-Fe_3O_4@Pd/PDA exhibit typical superparamagnetic behavior. The saturation magnetization values of h-Fe_3O_4 and h-Fe_3O_4@Pd/PDA are 76 emu g^{-1} and 32 emu g^{-1}, respectively. Due to the presence of the non-magnetic PDA layer and Pd nanocrystals, the magnetic saturation property of h-Fe_3O_4@Pd/PDA was reduced. However, compared with previously reported magnetic catalysts such as Fe_3O_4@Gly (5 emu g^{-1}),[48] Fe_3O_4/TiO_2 (1.74 emu g^{-1}),[49] and CuS/Fe_3O_4 (24.4 emu g^{-1}),[50] the h-Fe_3O_4@Pd/PDA hollow sphere has a higher magnetic saturation which allows better magnetic separation. As a result, the h-Fe_3O_4@Pd/PDA hollow spheres should have remarkable magnetic recovery properties in nanocatalysis.

The surface chemical composition and binding state of h-Fe_3O_4@Pd/PDA hollow spheres were further analyzed by X-ray photoelectron spectroscopy (XPS). Full-scan spectra of h-Fe_3O_4@Pd/PDA hollow spheres exhibit the typical C 1s, Fe 2p, O 1s, N 1s, and Pd 3d signals (Fig. 4a). The peaks of O 1s (532.17 eV) and Fe 2p (710.9 eV) are attributed to h-Fe_3O_4 and the C 1s (284.8 eV) is mainly attributed to residual polyacrylamide chains or ethanol. When the h-Fe_3O_4 core surface is coated by a Pd/PDA shell, Pd 3d (335.5 eV) and N 1s (400.1 eV) appear. The peak strength of Fe 2p is critically reduced, which proves that the h-Fe_3O_4 core is well encapsulated by the Pd/PDA hybrid shell. The Fe 2p peaks at h-Fe_3O_4@Pd/PDA are deconvoluted into five peaks (Fig. 4b). The peaks at 710.6, 712.7, 724.6 and 731 eV belong to Fe^{2+} $2p_{3/2}$, Fe^{3+} $2p_{3/2}$, Fe^{2+} $2p_{1/2}$, and Fe^{3+} $2p_{1/2}$, respectively, while 717.3 eV is the satellite peak. The N 1s peak can be deconvoluted

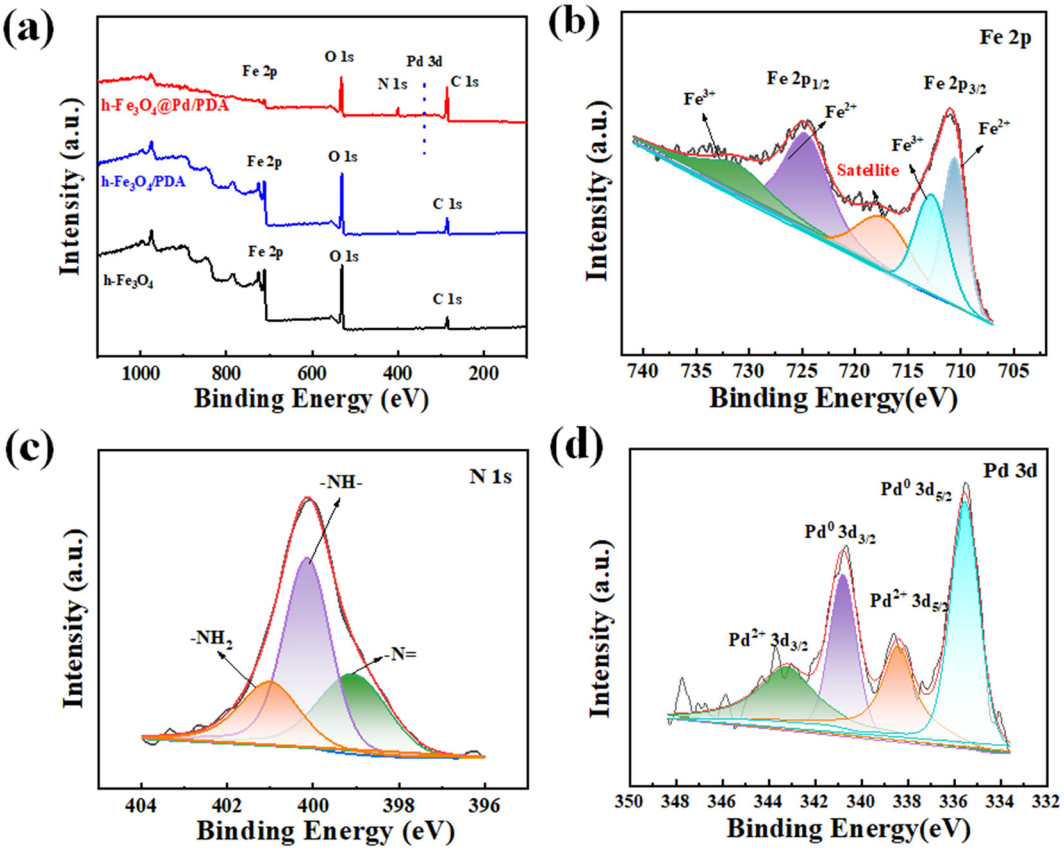

Fig. 4 XPS spectra of h-Fe_3O_4, h-Fe_3O_4/PDA, and h-Fe_3O_4@Pd/PDA (a). Fe 2p (b), N 1s (c) and Pd 3d (d) core-level spectra of h-Fe_3O_4@Pd/PDA.

into three peaks (Fig. 4c), and the peaks at 399.07, 400.14 and 401 eV belong to the tertiary/aromatic (–N═), secondary (–NH–), and primary (–NH_2) amine groups of PDA, respectively. More importantly, a weak Pd peak is found in the product, which must be attributed to the thin coating layer of the PDA shell. The Pd 3d spectrum of h-Fe_3O_4@Pd/PDA shows a pair of spin–orbit doublets corresponding to Pd $3d_{5/2}$ and Pd $3d_{3/2}$ (Fig. 4d). Here, the Pd^0 at 335.5 and 340.8 eV are the Pd^0 $3d_{5/2}$ and Pd^0 $3d_{3/2}$, respectively. In addition, Pd^{2+} $3d_{5/2}$ and Pd^{2+} $3d_{3/2}$ peaked at 338.4 and 343.2 eV, respectively. The presence of Pd^{2+} can be attributed to the adsorption of excess Pd^{2+} precursors on the h-Fe_3O_4@Pd/PDA hollow spheres. The difference in intensity between Pd^{2+} and Pd^0 demonstrates that the Pd element encapsulated within the PDA shell is Pd^0.

Reasonable adjustment of synthesis routes is becoming increasingly important for tuning the shape and size of nanoparticles for the purpose of catalytic applications.[51] Fig. 5 and 6 show the influencing factors for h-Fe_3O_4@Pd/PDA hollow spheres. Without using the h-Fe_3O_4 hollow spheres as the nanocarrier, the Pd nanoparticles are easily aggregated to form clusters, which are also coated by the gray and white PDA layers (Fig. 5a and b). Here, pristine h-Fe_3O_4 hollow spheres without surface modification are used as carriers, and the Pd nanoparticles can be immobilized on the surface of the hollow spheres. However, these nanoparticles are still aggregated on the h-Fe_3O_4 hollow spheres due to the weak interaction (Fig. 5c and d). APTES has been widely used as a grafting agent to promote the interfacial behavior of magnetic iron oxide nanoparticles, which can provide rich anchoring sites to trap individual atoms/clusters and prevent agglomeration.[52] Therefore, APTES was applied to graft the h-Fe_3O_4 hollow spheres, and then the Pd nanocrystals could be uniformly dispersed on the h-Fe_3O_4 hollow spheres (Fig. 5e and f). In addition, the final morphology of noble metal nanocrystals was also affected by different stabilizers. Monodisperse Pd metal nanocrystals can be synthesized by adding sodium citrate as a stabilizer to the ethanol solution of h-Fe_3O_4-APTES. The size of the Pd nanocrystals is about 10.7 nm (Fig. S2a†). Here, with the help of polyvinylpyrrolidone (PVP) as a stabilizer, the Pd nanocrystals can be uniformly self-assembled on the surface of h-Fe_3O_4 hollow spheres without any chemical function (Fig. 5g and h), By improving the dispersion, the size of the synthesized Pd nanocrystals becomes uniform and reduces to about 3.4 nm (Fig. S2b†). However, the reaction time of PVP synthesis is longer than that of the first method.

The concentration of H_2PdCl_4 also has an important effect on the final product. When the H_2PdCl_4 concentration (0.01 M, 4.4 mL) is low, the content of Pd nanocrystals wrapped in the PDA layer is relatively less, so only a few Pd nanoparticles

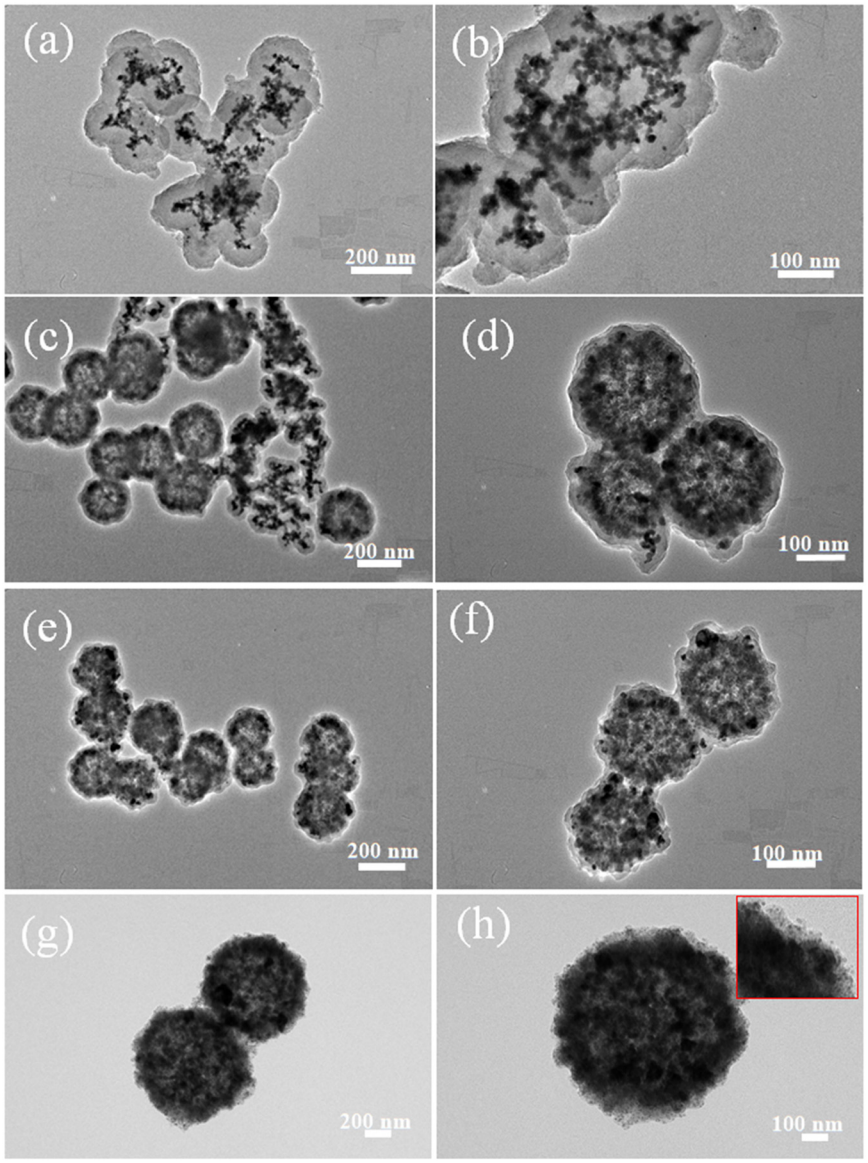

Fig. 5 TEM images of Pd nanoparticles without carrier (a and b), h-Fe_3O_4@Pd/PDA prepared without APTES modification (c and d), h-Fe_3O_4@Pd/PDA prepared with APTES modification (e and f), h-Fe_3O_4@Pd/PDA prepared with PVP as a stabilizer (g and h).

can be fixed on the h-Fe_3O_4 core (Fig. 6a and d). In this case, the content of Pd nanocrystals determined by ICP-AES is 13.2 wt% (Table S1†). As the concentration of H_2PdCl_4 increased (0.01 M, 8.8 mL), the number of Pd nanocrystals sandwiched between the PDA layer and h-Fe_3O_4 increased (Fig. 6b and e). At this time, the content of Pd nanocrystals is 19.3 wt% (Table S1†). When the H_2PdCl_4 concentration reached 13.2 mL, the density of Pd nanoparticles increased to the point that the hollow structure of h-Fe_3O_4 hollow spheres almost disappeared (Fig. 6c and f). At this point, the Pd nanocrystal content is 24.7 wt% (Table S1†). However, in this case, large aggregation of h-Fe_3O_4@Pd/PDA hollow spheres was easily obtained. Therefore, based on the above analysis, h-Fe_3O_4@Pd/PDA hollow spheres can be prepared by modifying h-Fe_3O_4 with APTES and selecting an optimum Pd content (0.01 M, 8.8 mL). Actually, the preparation of h-Fe_3O_4@Pd/PDA hollow spheres by redox-oxidative polymerization is simple, which solves the problems of complicated synthesis procedures for the three-layered core–shell nanostructure. Owing to the good separation and recovery of the Pd catalyst, the h-Fe_3O_4@Pd/PDA hollow sphere has a wide application prospect in nanocatalysis.

Actually, this *in situ* coating is simple and universal, and it can be further extended to synthesize other kinds of immobilized noble metal nanocrystals with different carriers (Fig. 7 and 8). Typically, the h-Fe_3O_4@Au/PDA hollow spheres can be easily obtained. Shown in Fig. 7a and b are TEM images of h-Fe_3O_4@Au/PDA. Au nanocrystals are evenly dispersed on h-Fe_3O_4 hollow spheres and they are clearly covered by another layer of PDA shell. Moreover, when $Ag(NH_3)_2OH$ was applied as the

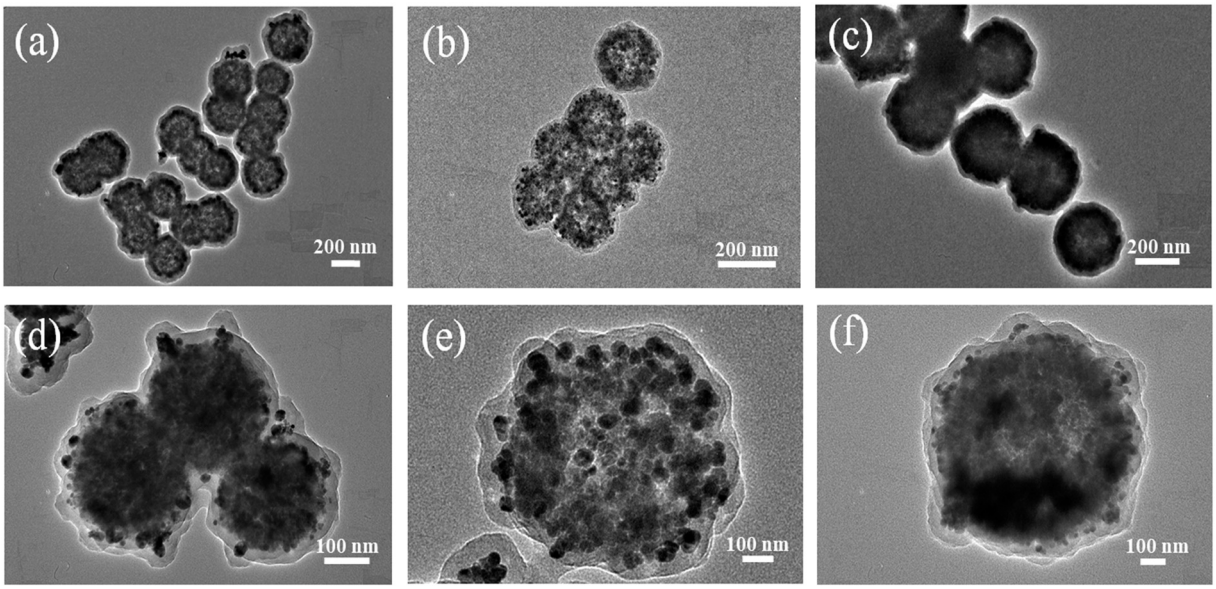

Fig. 6 TEM images of h-Fe_3O_4@Pd/PDA prepared with different content of H_2PdCl_4: 4.4 × 10^{-5} mol (a and d), 8.8 × 10^{-5} mol (b and e) and 13.2 × 10^{-5} mol (c and f).

noble metal source, h-Fe_3O_4@Ag/PDA can be synthesized (Fig. 7c and d). Due to the quick Ostwald maturation process,[53] the Ag nanocrystals on h-Fe_3O_4 hollow spheres are not uniform, both small Ag nanocrystals and large irregular Ag nanocrystals will be formed.

When MXene nanosheets were used as the carrier material, the Pd nanocrystals were uniformly dispersed on the MXene nanosheets (Fig. 8a and b). Due to the high affinity of the surface functional groups of MXene, a large number of Pd nanocrystals can be immobilized on the nanosheets.[47] Similarly, Pd nanocrystals can be uniformly distributed on SiO_2 nanospheres in a linear manner to form SiO_2@Pd/PDA nanospheres (Fig. 8c and d). Besides the spherical nanocarrier, this method is also effective for carrying Pd nanocrystals on non-spherical ones. Here, α-Fe_2O_3 nanoellipsoids were applied to fabricate α-Fe_2O_3@Pd/PDA core–shell hybrid materials. As shown in Fig. 8e and f, Pd nanocrystals are uniformly dispersed on α-Fe_2O_3 nanoellipsoids in a raindrop shape. In conclusion, the synthesis method is universal and can be extended for carrying different nanocatalysts on different nanocarriers.

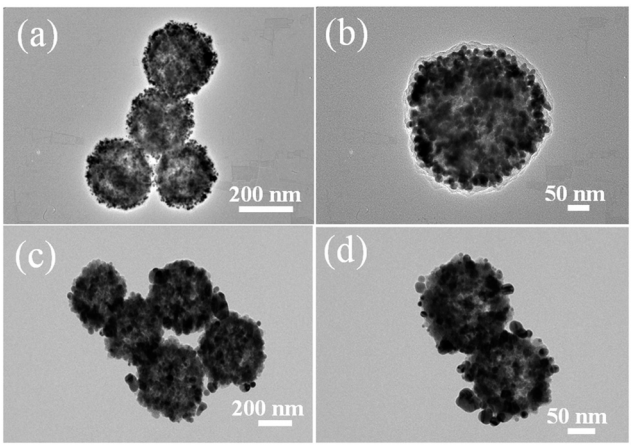

Fig. 7 TEM images of h-Fe_3O_4@Au/PDA hollow spheres (a and b); h-Fe_3O_4@Ag/PDA hollow spheres (c and d).

3.2. Photothermal properties of h-Fe_3O_4@Pd/PDA hollow spheres

The h-Fe_3O_4@Pd/PDA hollow spheres also show good photothermal properties. Firstly, the absorption spectra of h-Fe_3O_4 and h-Fe_3O_4@Pd/PDA hollow spheres at 808 nm are measured. It can be seen that in the near-infrared region, the light absorption of h-Fe_3O_4@Pd/PDA hollow spheres is significantly higher than that of h-Fe_3O_4 with the same concentration (Fig. 9a), which was due to the enhanced near-infrared absorption properties of Pd nanocrystals and the PDA protective layer. According to the Lambert–Beer law,[54] the extinction coefficients of h-Fe_3O_4@Pd/PDA was 10.51 L g^{-1} cm^{-1}, which is higher than that of h-Fe_3O_4 and h-Fe_3O_4/PDA. Thus, h-Fe_3O_4@Pd/PDA can be used as an ideal photothermal reagent (Fig. 9b). Fig. 9c shows the heating and cooling curves of different components, in which an infrared camera was used to monitor the temperature change, and the specific method is shown in section 2.3. The temperature of h-Fe_3O_4@Pd/PDA hollow spheres (100 μg mL^{-1}) reached 70.8 °C after 6 min irradiation by NIR laser (808 nm, 2.0 W cm^{-2}). Under the same heating conditions and concentrations, the temperature of h-Fe_3O_4 and h-Fe_3O_4/PDA reached only 57.4 °C and 66.4 °C, respectively. The difference in temperature must be attributed to the contributions of h-Fe_3O_4 and PDA as well as the localized surface plasmon resonance effect of Pd nanocrystals.

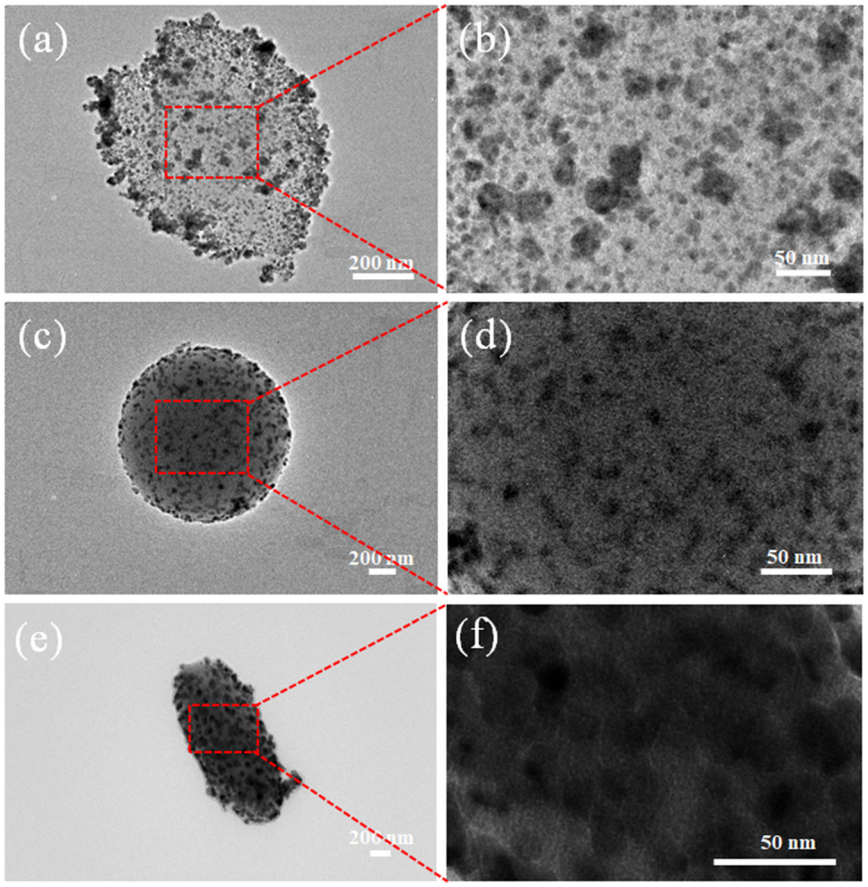

Fig. 8 TEM images of MXene@Pd/PDA nanosheets (a and b), SiO_2@Pd/PDA nanospheres (c and d), α-Fe_2O_3@Pd/PDA nanoellipsoids (e and f).

Fig. 9d shows the photothermal conversion temperature of h-Fe_3O_4@Pd/PDA under different concentrations. It is found that the temperature reaches as high as 70.8 °C when the concentration increases to 100 μg mL^{-1}. To study the photothermal conversion efficiency of h-Fe_3O_4@Pd/PDA hollow spheres (100 μg mL^{-1}) accurately, the heating and cooling curve of h-Fe_3O_4@Pd/PDA hollow spheres (100 μg mL^{-1}) was recorded, and the photothermal conversion efficiency (η) was calculated to be 31.30%. The inset is a linear fitting curve of the negative natural logarithm of the cooling time and the driving temperature (Fig. 9e). As shown in Fig. 9f, no significant change in temperature distribution of h-Fe_3O_4@Pd/PDA was observed in the 6 light cycles under NIR laser (808 nm, 2.0 W cm^{-2}), which proves that h-Fe_3O_4@Pd/PDA has good photothermal cycling stability. Obviously, h-Fe_3O_4@Pd/PDA has good photothermal conversion efficiency and photothermal stability. Fig. 9g shows the infrared thermal image of h-Fe_3O_4@Pd/PDA (100 μg mL^{-1}) suspensions irradiated by NIR light for 6 min. The color of the solution gradually changes from blue (corresponding to low temperature) to bright yellow (corresponding to high temperature), which clearly demonstrates that the temperature increases with the increase of irradiation time.

3.3. Catalytic activity of h-Fe_3O_4@Pd/PDA hollow spheres on selective reductive hydrogenation of 4-nitrostyrene

Originating from the Pd nanoparticles, the h-Fe_3O_4@Pd/PDA hollow spheres show excellent catalytic activity. Aniline is an important intermediate for the industrial synthesis of various pesticides, drugs, dyes and pigments. For the hydrogenation of nitroaromatic hydrocarbons with coexisting competitive unsaturated functional groups, it is still a great challenge to obtain ideal hydrogenation products, especially 4-nitrostyrene.[55] Catalytic hydrogenation of 4-nitrostyrene may produce three products, namely 4-aminostyrene, 4-nitroethylbenzene and 4-ethylaniline. 4-Nitrostyrene and the other three products have absorption peaks at 311 nm, 273 nm, 280 nm and 234 nm in the UV-vis absorption spectra. Therefore, UV-vis spectroscopy can be used to monitor the conversion process of 4-nitrostyrene (Fig. 10a). Fig. 10b shows the transformation curve of 4-nitrostyrene at room temperature for 1 h. The absorption peak of 4-nitrostyrene (311 nm) is weakened, and the absorption peak at 311 nm is blue-shifted to the short wave. This indicates that 4-nitrostyrene is reacting, and the reaction is proceeding very slowly.

Due to the remarkable photothermal behavior, this reaction can be conducted under NIR irradiation by using

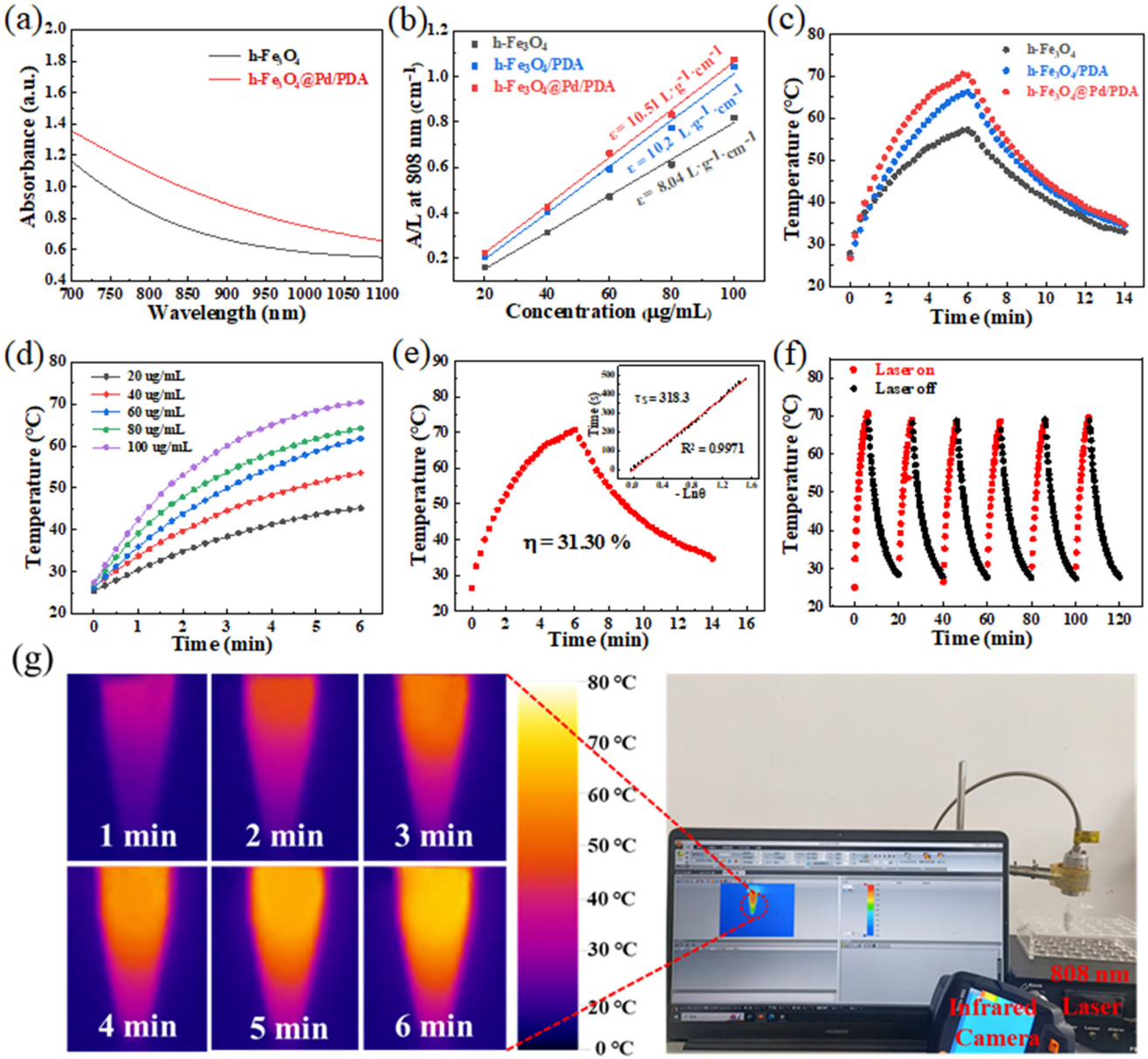

Fig. 9 Photothermal property characterization of the h-Fe_3O_4@Pd/PDA hollow spheres under NIR light irradiation (808 nm, 2.0 W cm^{-2}): UV-vis absorption spectra of h-Fe_3O_4@Pd/PDA hollow spheres (a). Mass extinction coefficient of h-Fe_3O_4, h-Fe_3O_4/PDA, and h-Fe_3O_4@Pd/PDA (b). Continuous irradiation for 6 min and natural cooling curves of h-Fe_3O_4, h-Fe_3O_4/PDA, and h-Fe_3O_4@Pd/PDA (average concentration 100 μg mL^{-1}) (c). Heating curves of continuous irradiation for 6 min of h-Fe_3O_4@Pd/PDA at different concentrations (d). Temperature curves of h-Fe_3O_4@Pd/PDA hollow spheres (100 μg mL^{-1}) after continuous irradiation for 6 min and natural cooling and a plot fitting of cooling time *versus* −ln(θ) (inset graph) (e). Heating and cooling curves for 6 laser on/off cycles of the h-Fe_3O_4@Pd/PDA hollow spheres (f). Infrared image of h-Fe_3O_4@Pd/PDA (100 μg mL^{-1}) suspensions under NIR laser irradiation (g).

our h-Fe_3O_4@Pd/PDA nanocatalyst. Fig. 10c shows the reaction of 4-nitrostyrene catalyzed by h-Fe_3O_4@Pd/PDA (8 mg) under a NIR laser (808 nm, 2.0 W cm^{-2}), The absorption peak of 4-nitrostyrene at 311 nm decreased, and that of 4-aminostyrene at 273 nm increased, indicating that 4-nitrostyrene was gradually converted to 4-aminostyrene, and the catalytic reaction was completed in 40 min. Importantly, the NIR radiation can obviously accelerate the reaction. In this work, accurately verified by GC-MS, it is found that h-Fe_3O_4@Pd/PDA shows good selectivity for 4-nitrostyrene to 4-aminophenylene. During the reaction, it is found that the conversion rate is 78.3%, and the selectivity of 4-nitrostyrene to 4-aminophenylene reaches as high as 84.8% (Fig. 10d). As a result, the h-Fe_3O_4@Pd/PDA nanocatalyst shows both high catalytic activity and selectivity under NIR irradiation.

The effect of catalyst content on the reaction was further investigated. With the concentration of NH_3BH_3 unchanged, when the catalyst dosage was 4 mg, 8 mg and 12 mg, the reaction was completed in 70 min, 40 min and 25 min,

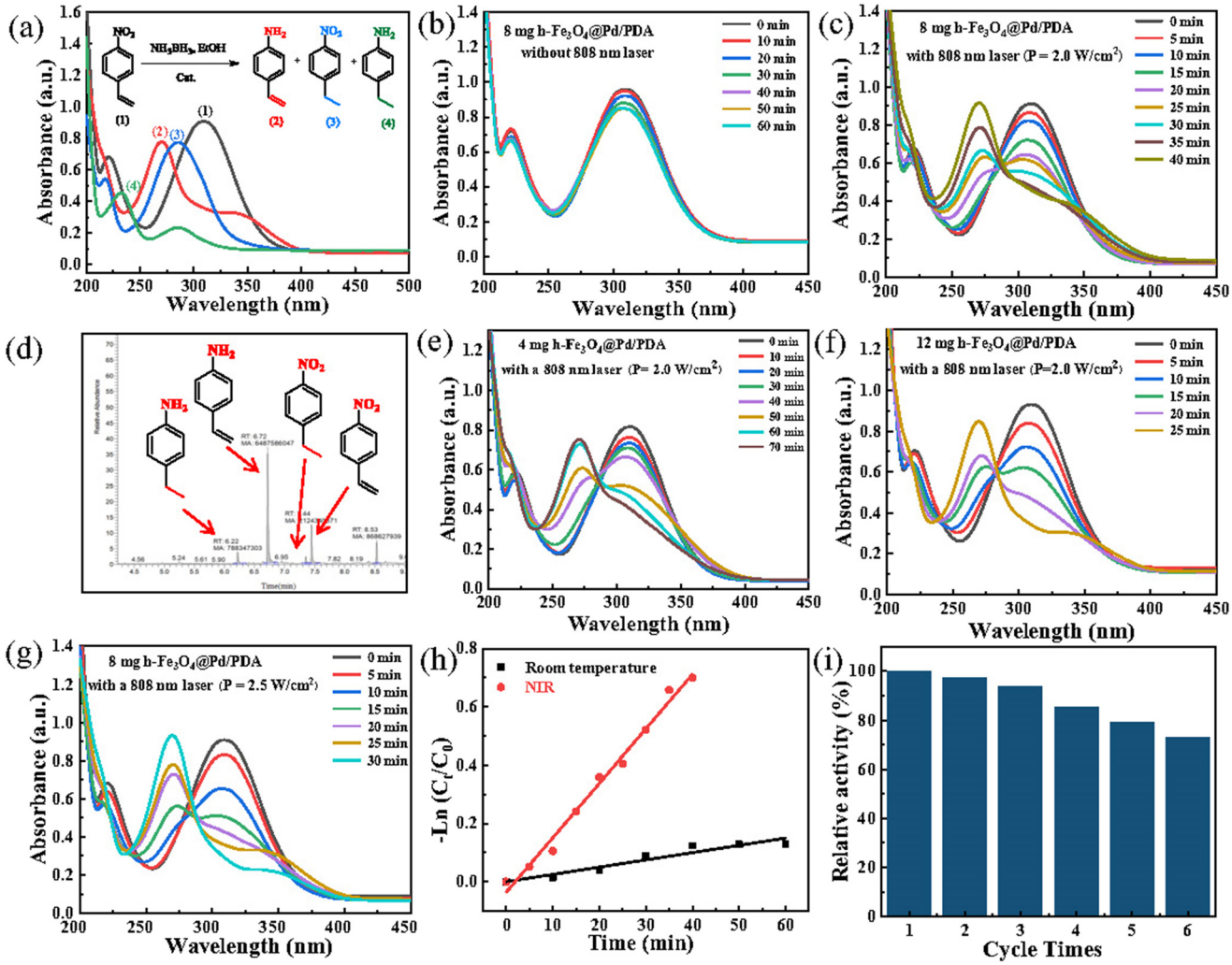

Fig. 10 UV-vis absorption spectra of h-Fe_3O_4@Pd/PDA catalytic reduction of 4-nitrostyrene: UV-vis absorption spectra of (1) 4-nitrostyrene, (2) 4-aminostyrene, (3) 4-nitroethylbenzene and (4) 4-ethylaniline (a). UV-vis spectra of 4-nitrostyrene catalyzed by h-Fe_3O_4@Pd/PDA for 1 h at room temperature (b). UV-vis spectra of 4-nitrostyrene catalyzed by h-Fe_3O_4@Pd/PDA (8 mg) under NIR laser (808 nm, 2.0 W cm^{-2}) irradiation (c). GC-MS spectrum of the product after catalytic reaction (d). UV-vis spectra of 4-nitrostyrene catalyzed by h-Fe_3O_4@Pd/PDA with different contents under NIR laser (808 nm, 2.0 W cm^{-2}) irradiation: 4 mg (e), 12 mg (f). UV-vis spectra of 4-nitrostyrene catalyzed by h-Fe_3O_4@Pd/PDA (8 mg) under NIR laser (808 nm, 2.5 W cm^{-2}) irradiation (g). Linear relationship between $-\ln(C_t/C_0)$ and reaction time of nanocatalysts under different conditions (h). Six cycles of catalytic testing (i).

respectively (Fig. 10c, e and f). Thus, the amount of catalyst also has an important effect on the conversion of 4-nitrostyrene, demonstrating a pseudo-first-order kinetics. By using 8 mg h-Fe_3O_4@Pd/PDA as a catalyst to catalyze the conversion of 4-nitrostyrene, under 2.5 W cm^{-2} 808 nm NIR laser, the catalytic reaction could be completed within 30 min (Fig. 10g), which indicates that high NIR intensity can induce quicker reaction dynamics.

To investigate the NIR-improved mechanism, the photothermal behavior of the catalytic procedure was examined. Fig. 10h shows the influence of different reaction conditions on the reaction kinetics. Since excessive NH_3BH_3 ensured a constant NH_3BH_3 concentration during the reaction, in order to study the reaction kinetics of the catalyst, a pseudo-first-order kinetic model was adopted to draw the relationship between $-\ln(C_t/C_0)$ and the reaction time t, where k_a was the reaction rate constant. The reaction rate constant k_a of the catalyst under NIR laser is 0.019 min^{-1}. Compared with that at room temperature (0.002 min^{-1}), the reaction rate under NIR laser irradiation is faster. The enhancement of catalytic activity under NIR laser irradiation must be attributed to the photothermal and plasmon resonance properties of Pd nanocrystals. As a result, this work developed an easy initiation method for the catalytic hydrogenation of 4-nitrostyrene. The cyclic catalytic activity of h-Fe_3O_4@Pd/PDA in the chemical selective hydrogenation of 4-nitrostyrene was further tested (Fig. 10i). After 6 cycles, the catalytic activity of h-Fe_3O_4@Pd/PDA was still higher than 70%, indicating that the catalyst has a good catalytic cycle activity for 4-nitrostyrene.

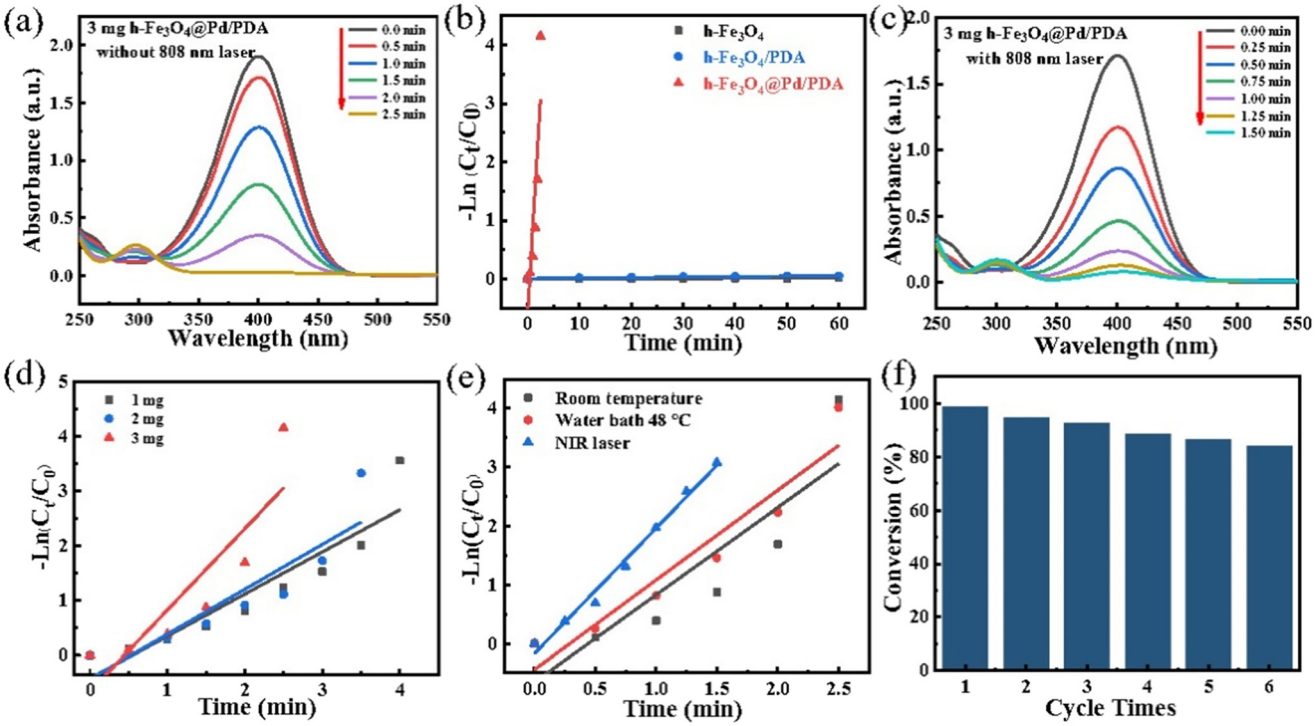

Fig. 11 Performance characterization of h-Fe_3O_4@Pd/PDA catalytic reduction of 4-nitrophenol: UV-vis spectra of 4-nitrophenol catalyzed by h-Fe_3O_4@Pd/PDA hollow spheres (3 mg) at room temperature (a). Linear relationship between $-\ln(C_t/C_0)$ and the reaction time of 4-nitrophenol catalyzed by h-Fe_3O_4, h-Fe_3O_4/PDA, and h-Fe_3O_4@Pd/PDA hollow spheres (the contents are all 3 mg) (b). UV-vis spectra of 4-nitrophenol catalyzed by h-Fe_3O_4@Pd/PDA hollow spheres under NIR laser (808 nm, 2.0 W cm^{-2}) irradiation (c). Linear relationship between $-\ln(C_t/C_0)$ and reaction time of nanocatalysts with different contents (d). Linear relationship between $-\ln(C_t/C_0)$ and reaction time of nanocatalysts under different conditions (e). Six cycles of catalytic reduction of 4-nitrophenol by h-Fe_3O_4@Pd/PDA at room temperature (f).

3.4. Catalytic activity of h-Fe_3O_4@Pd/PDA hollow spheres on 4-nitrophenol

4-Nitrophenol widely exists in the wastewater of printing, textile, petrochemical and other industries. It has a destructive effect on the ecological environment and human health. Moreover, a reduction product of 4-nitrophenol, 4-aminophenol, acts as an intermediate in the synthesis of many analgesic and antipyretic drugs.[56] Here, the catalytic activity of h-Fe_3O_4@Pd/PDA hollow spheres on 4-nitrophenol was investigated. As shown in Fig. S3,† when only 4-nitrophenol was present in the solution, the absorption peak appeared at 317 nm, and the solution was pale yellow. After the addition of $NaBH_4$, 4-nitrophenol was converted to 4-nitrophenol ion, and the absorption peak was red-shifted to 400 nm. At the same time, the solution turned bright yellow. With the further addition of the catalyst, the ions were converted to 4-aminophenol, the absorption peak shifted to 300 nm, and the solution gradually became transparent. Fig. 11a shows the time-dependent absorption curves of h-Fe_3O_4@Pd/PDA hollow spheres on the catalytic reduction of 4-nitrophenol at room temperature. As the reaction continues, the absorption peak of 4-nitrophenol at 400 nm is weakened and the absorption peak at 300 nm is increased, indicating that 4-nitrophenol is gradually converted to 4-aminophenol, and the reaction is almost completed in 2.5 min. Since excess $NaBH_4$ ensured the constant concentration of $NaBH_4$ during the reaction, in order to study the reaction kinetics of the catalyst, a pseudo-first-order kinetic model was adopted to draw the relationship between $-\ln(C_t/C_0)$ and the reaction time t, where k_a was the reaction rate constant. The effects of different catalysts on the reaction kinetics were investigated (Fig. 11b). The reaction rate constants k_a for 4-nitrophenol at the same concentration of h-Fe_3O_4, h-Fe_3O_4/PDA and h-Fe_3O_4@Pd/PDA are 3.02×10^{-4} min^{-1}, 8.15×10^{-4} min^{-1}, and 1.49 min^{-1}, respectively. Obviously, only h-Fe_3O_4@Pd/PDA shows the typical catalytic activity for 4-nitrophenol.

Interestingly, h-Fe_3O_4@Pd/PDA shows a unique NIR-improved catalytic activity. Fig. 11c shows time-dependent absorption curves of h-Fe_3O_4@Pd/PDA hollow spheres on the

Table 1 Comparison of the reduction of 4-nitrophenol with different catalysts

Catalysts	Mass (mg)	k_a (min^{-1})	k_n (min^{-1} mg^{-1})	References
Ag/LDH-ITA-GG NC	1	0.2142	0.2142	57
Pd/PVP-PS	20	0.0590	0.00295	58
$MoNi_4$–MoO_2	2.5	0.445	0.178	59
Pd@g-CN	5	1.562	0.312	60
$Ag_3PO_4/Fe_3O_4/C_{60}$	2.5	0.1225	0.049	61
h-Fe_3O_4@Pd/PDA	1	0.77	0.77	This work

catalytic reduction of 4-nitrophenol under NIR laser irradiation (808 nm, 2.0 W cm^{-2}). The catalytic reaction could be completed in 1.5 min, which is much quicker than the one without using NIR irradiation. The effects of catalyst content on reaction kinetics were investigated (Fig. 11d); the reaction rate constants k_a of 1 mg, 2 mg and 3 mg h-Fe_3O_4@Pd/PDA hollow spheres are 0.77 min^{-1}, 0.82 min^{-1}, and 1.49 min^{-1}, respectively. The rate constant k_n values are 0.77 min^{-1} mg^{-1}, 0.41 min^{-1} mg^{-1}, and 0.496 min^{-1} mg^{-1}, which are better than that of the previously reported nanocatalysts (Table 1).

Moreover, the effects of reaction conditions (non-NIR, NIR, water bath) on reaction kinetics were investigated. As shown in Fig. 11e, under the irradiation of a NIR laser (808 nm, 2.0 W cm^{-2}), the reaction rate constant k_a increased to 2.13 min^{-1}, while the reaction rate constant k_a was 1.49 min^{-1} at room temperature and 1.53 min^{-1} at 48 °C in a water bath. The setting temperature of the water bath was set according to the heating curve of the reaction under NIR laser (808 nm, 2.0 W cm^{-2}) irradiation (Fig. S4†). Obviously, for the reactions that can occur at room temperature (such as the catalysis of 4-nitrophenol), photothermal heating has a weak effect on improving the catalytic activity, and the catalytic enhancement under NIR light is mainly due to the Pd nanocrystalline plasmon resonance effect. Fig. 11f shows the cyclic catalytic activity of h-Fe_3O_4@Pd/PDA hollow spheres. After 6 cycles, the catalytic activity of h-Fe_3O_4@Pd/PDA hollow spheres for 4-nitrophenol is still higher than 80%, indicating that the catalyst has good cyclic catalytic activity.

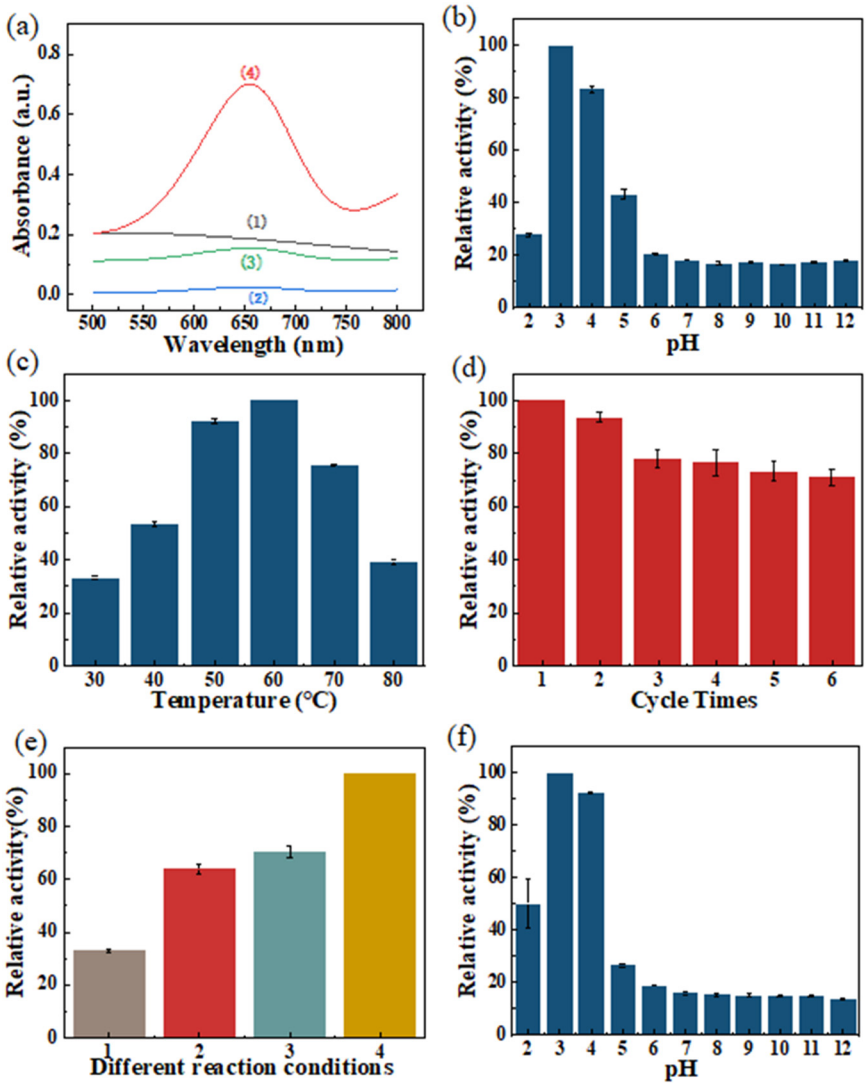

Fig. 12 Typical UV-vis spectra of the different components in an HAc–NaAc buffer solution: (1) h-Fe_3O_4@Pd/PDA, (2) TMB + H_2O_2, (3) TMB + H_2O_2 + h-Fe_3O_4 and (4) TMB + H_2O_2 + h-Fe_3O_4@Pd/PDA (a). The factors affecting the peroxidase-like activity of h-Fe_3O_4@Pd/PDA: pH (b), temperature (c). The reusability of h-Fe_3O_4@Pd/PDA (d). The effects of different heating conditions on the peroxidase activity of h-Fe_3O_4@Pd/PDA: (1) reaction at room temperature for 10 min, (2) NIR laser (808 nm, 2.0 W cm^{-2}) irradiation for 10 min, (3) NIR laser (808 nm, 2.0 W cm^{-2}) irradiation and heating to 60 °C, (4) water bath at 60 °C for 10 min (e). The effect of different pH on the peroxidase activity of h-Fe_3O_4@Pd/PDA under NIR reaction condition (f).

3.5. Catalytic activity of h-Fe_3O_4@Pd/PDA hollow spheres for TMB

Besides the reducing reaction, the h-Fe_3O_4@Pd/PDA hollow spheres also exhibit unique catalytic activity on the peroxidase activity. 3,3′,5,5′-Tetramethylbenzidine (TMB), as a substrate of peroxidase, is commonly used to detect biomarkers of various diseases.[62–64] h-Fe_3O_4@Pd/PDA hollow spheres have no absorption peak in the wavelength range 500–800 nm (inset 1 of Fig. 12a). When TMB + H_2O_2 is added in the reaction system, there is almost no absorption peak at 652 nm after 10 min of reaction in a water bath at 60 °C (inset 2 of Fig. 12a). When h-Fe_3O_4 is used as the catalyst, the absorption peak of ox-TMB can be seen at 652 nm, but the peak is relatively weak (inset 3 of Fig. 12a). When h-Fe_3O_4@Pd/PDA hollow spheres are used as the catalyst, there is a significant ox-TMB absorption peak at 652 nm, which indicates that it shows a good peroxidase-like catalytic activity (inset 4 of Fig. 12a). Temperature and pH are important factors affecting the catalytic effect of H_2O_2 oxidation of TMB catalyzed by peroxidase or natural enzyme.[65] Therefore, the optimal pH and temperature for the catalytic oxidation of TMB by h-Fe_3O_4@Pd/PDA hollow spheres were investigated. It is found that when pH increases from 2 to 3, the catalytic activity of h-Fe_3O_4@Pd/PDA hollow spheres increases. When pH increases from 3 to 12, the catalytic activity of h-Fe_3O_4@Pd/PDA gradually decreases, so the optimal pH of the reaction system is 3 (Fig. 12b). As shown in Fig. 12c, the catalytic activity of h-Fe_3O_4@Pd/PDA firstly increases with the temperature and then decreases, so the catalytic activity is the highest when the temperature is 60 °C. Through the above experiments, it can be determined that the optimal temperature of h-Fe_3O_4@Pd/PDA hollow spheres catalyzing the H_2O_2 oxidation of TMB is 60 °C and the optimal pH is 3.0, which are used as standard reaction conditions for subsequent experiments. Fig. 12d further investigates the catalytic cycling activity of h-Fe_3O_4@Pd/PDA hollow spheres for TMB. Due to the extremely low concentration of the catalyst (20 μg mL^{-1}) in the reaction, there is an inevitable quality loss during the recovery process, resulting in a decrease in catalytic activity. However, the catalytic activity remains above 70% after 6 consecutive cycles, which indicates that the product has good recyclability.

NIR laser irradiation is a simple, rapid, convenient and environmentally adaptable method. Since h-Fe_3O_4@Pd/PDA has good photothermal activity, NIR irradiation was used to further investigate the catalytic oxidation of TMB (Fig. 12e and f). The catalytic activities of h-Fe_3O_4@Pd/PDA at

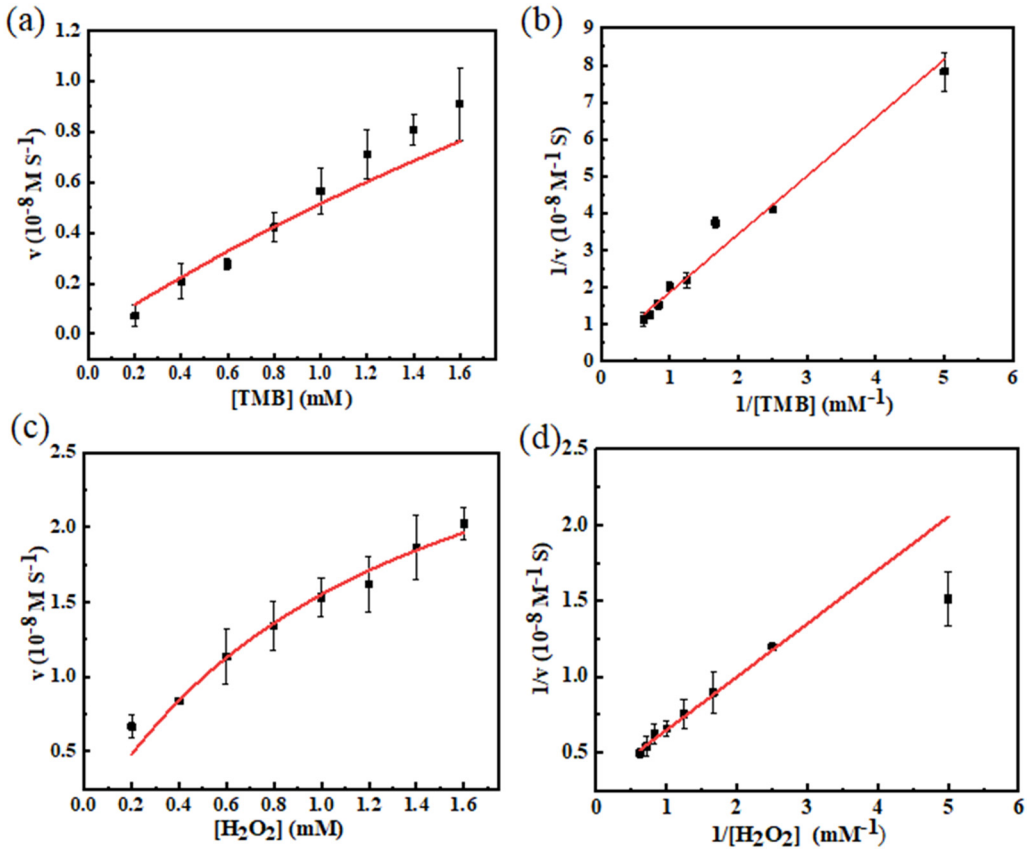

Fig. 13 Steady-state kinetic assays of h-Fe_3O_4@Pd/PDA: the concentration of H_2O_2 was fixed and the velocity varied with the concentration of TMB (a). The Lineweaver-Burk plot with varying TMB and fixed H_2O_2 concentration (b). The concentration of TMB was fixed and the velocity varied with the concentration of H_2O_2 (c). The Lineweaver–Burk plot with varying H_2O_2 and fixed TMB concentration (d).

room temperature (10 min), NIR (10 min), NIR (60 °C) and water bath (60 °C) for the oxidation of TMB were investigated (Fig. 12e). Compared with room temperature, NIR treatment significantly improved the catalytic TMB reaction, but the reaction activity was still lower than that of the water bath treatment at 60 °C. This is due to the fact that the optimum temperature for catalyzing TMB is 60 °C (Fig. 12c). Near-infrared irradiation is continuously heated, but not fixed at 60 °C. Therefore, the TMB catalytic activity of the NIR treatment at 60 °C is lower than that of the water bath treatment at 60 °C. However, when the reaction environment is harsh and cannot be heated directly by a water bath, NIR laser treatment can be an effective heating method. In addition, the effect of pH on the NIR laser catalytic reaction was also investigated. As shown in Fig. 12f, similar to water bath conditions, pH 3.0 is still the optimal pH for catalytic reactions. In conclusion, for some high-temperature reactions, the photothermal effect is the main factor affecting the catalytic activity, and the Pd metal plasmon resonance effect of h-Fe_3O_4@Pd/PDA is not obvious.

With H_2O_2 and TMB as substrates, a series of experiments were carried out to study the steady-state kinetic parameters of h-Fe_3O_4@Pd/PDA peroxidase. The relationship between substrate concentration and initial reaction rate follows the typical Michaelis–Menten curve. The corresponding Lineweaver–Burk double reciprocal graph was drawn. When the concentration of H_2O_2 is fixed and the concentration of TMB was changed, K_m is 5.36 and V_{max} is 3.42 (Fig. 13a and b). When TMB concentration is fixed and H_2O_2 concentration is changed, K_m is 1.18 and V_{max} is 3.35 (Fig. 13c and d). In summary, in the presence of H_2O_2, h-Fe_3O_4@Pd/PDA hollow spheres can be used as a peroxidase-like nanoenzyme to catalyze the oxidation of the chromogenic substrate 3,3′,5,5′-tetramethylbenzidine (TMB) to a blue substance (ox-TMB).

Based on the above analysis, the multi-mode NIR-improved catalytic performance of h-Fe_3O_4@Pd/PDA was proposed. Scheme 1 shows the hypothesized mechanism of h-Fe_3O_4@Pd/PDA hollow spheres for catalyzing the reduction of 4-nitrophenol and 4-nitrostyrene, and the oxidation of TMB. In aqueous solution, $NaBH_4$ ionizes to produce BH_4^-, which can react with the surface of bimetallic nanoparticles to generate active surface hydrogen and form Pd–H active substance. 4-Nitrophenol was adsorbed on the surface of Pd metal nanoparticles. Thus, BH_4^- acts as an electron donor, while 4-nitrophenol acts as an electron acceptor. Pd metal nanoparticles act as electronic relays to transfer surface hydrogen to 4-nitrophenol, resulting in the formation of 4-aminophenol. Finally, the product is desorption-separated from the surface of Pd metal nanoparticles to form a free surface, and the cyclic reduction reaction can be carried out again.[40,66] The catalytic mechanism of 4-aminostyrene is similar to the above analysis.[67] Under the irradiation of NIR light, Pd nanocrystals produce a plasmon resonance effect and produce more hot electrons. These hot electrons can overcome the Schottky barrier, inhibit the rapid

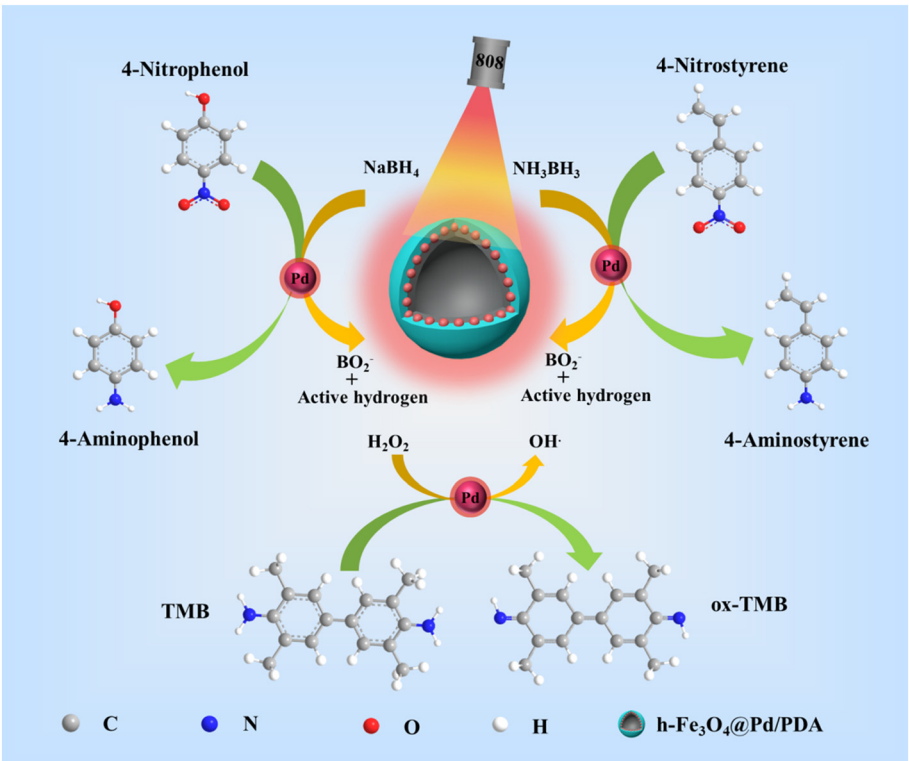

Scheme 1 Schematic illustration of the mechanism of h-Fe_3O_4@Pd/PDA hollow spheres for catalyzing the reduction of 4-nitrophenol and 4-nitrostyrene and the oxidation of TMB.

recombination of hot electron–hole pairs, and show the catalytic effect of photothermal enhancement. In addition, Pd nanocrystals have more holes after losing electrons and can accept more active hydrogen, thus accelerating the reduction of 4-nitrophenol and 4-nitrostyrene.[68] The catalytic TMB mechanism of h-Fe_3O_4@Pd/PDA may be due to the electron transfer from the lone pair in the TMB amino group to the Pd nanocrystals, and the Pd metal nanoparticles act as electronic relays, thus increasing the electron mobility and density of h-Fe_3O_4@Pd/PDA. The direct transfer of electrons from Pd nanoparticles to H_2O_2 is accelerated. It also effectively catalyzes the decomposition of H_2O_2 into $OH^{\bullet}$ radicals. Subsequently, $OH^{\bullet}$ radicals oxidize TMB to the blue product ox-TMB.[69] In summary, the h-Fe_3O_4@Pd/PDA hollow spheres have typical photothermally enhanced catalytic activity and universal applicability, which has a wide range of potential applications in the field of nanocatalysis.

4. Conclusion

In this work, a simple redox-oxidative polymerization method was developed for the preparation of magnetic h-Fe_3O_4@Pd/PDA hollow spheres. The h-Fe_3O_4@Pd/PDA hollow spheres exhibit excellent catalytic activity for 4-nitrostyrene, 4-nitrophenol and TMB. The conversion rate of 4-nitrostyrene to 4-aminostyrene reached 78.3%, the selectivity reached 84.8%, and the kinetic constant of 4-nitrophenol reached 0.77 min^{-1} mg^{-1}. In addition, NIR irradiation can improve the catalytic kinetics of the reaction when using h-Fe_3O_4@Pd/PDA as the catalyst. Under the irradiation of NIR light, Pd nanocrystals exhibit the plasmon resonance effect and produce more hot electrons. These hot electrons can overcome the Schottky barrier and inhibit the rapid recombination of hot electron–hole pairs. Pd nanocrystals have more holes after losing electrons and can accept more active hydrogen to form Pd–H bonds. The reduction of 4-nitrostyrene and 4-nitrophenol was accelerated, which showed the typical photothermal enhancing catalytic effect. The h-Fe_3O_4@Pd/PDA hollow spheres possess numerous advantages, including a straightforward synthesis method, excellent photothermal capabilities, effortless separation and reusability, and multifunctional catalytic activity across various reactions. This versatility render them highly applicable in nanocatalysis.

Conflicts of interest

The authors declare no conflict of interest.

Acknowledgements

Financial support from the National Natural Science Foundation of China (Grant No. 12072338, 52003003, 52003004) and the Fundamental Research Funds for the Central Universities (WK2480000007) is gratefully acknowledged.

References

1 F. Han, H. Zhang, C. Zhang, Y. Zhang, Y. Tang and X. Yang, *Sep. Purif. Technol.*, 2023, **325**, 124605.
2 F. Liu, X. Liu, F. Chen and Q. Fu, *J. Colloid Interface Sci.*, 2021, **604**, 281–291.
3 J. Rahimi, M. Naderi, M. Ijdani, M. Heidari, M. Azizi and A. Maleki, *Mater. Today Chem.*, 2023, **28**, 101375.
4 C. Hao, Y. Wang, S. Hu and X. Guo, *Appl. Catal., A*, 2023, **663**, 119326.
5 D. Yin, J. Zhang, W. Li and Y. Fu, *Catal. Lett.*, 2021, **151**, 1902–1910.
6 C. Biglione, A. L. Cappelletti, M. C. Strumia, S. E. Martín and P. M. Uberman, *J. Nanopart. Res.*, 2018, **20**, 1–16.
7 M. K. Das, J. A. Bobb, A. A. Ibrahim, A. Lin, K. M. AbouZeid and M. S. El Shall, *ACS Appl. Mater. Interfaces*, 2020, **12**, 23844–23852.
8 K. Karami, N. Jamshidian, M. M. Nikazma, P. Herves, A. R. Shahreza and A. Karami, *Appl. Organomet. Chem.*, 2018, **32**, e3978.
9 M. Nasrollahzadeh, T. Baran, N. Y. Baran, M. Sajjadi, M. R. Tahsili and M. Shokouhimehr, *Sep. Purif. Technol.*, 2020, **239**, 116542.
10 W. Li, T. Zhou, Z. Le, M. Liao, H. Liu, B. Na, B. Wang, H. Zhou and H. Yan, *RSC Adv.*, 2018, **8**, 35496–35502.
11 L. Polavarapu, S. Mourdikoudis, I. Pastoriza Santos and J. Perez Juste, *CrystEngComm*, 2015, **17**, 3727–3762.
12 R. M. Mironenko, O. B. Belskaya and V. A. Likholobov, *Catal. Today*, 2020, **357**, 152–165.
13 R. Nie, M. Chen, Y. Pei, B. Zhang, L. Qi, J. Chen, T. W. Goh, Z. Qi, Z. Zhang and W. Huang, *ACS Sustainable Chem. Eng.*, 2018, **7**, 3356–3363.
14 M. Çalışkan and T. Baran, *Int. J. Biol. Macromol.*, 2021, **174**, 120–133.
15 M. Celebi, M. Yurderi, A. Bulut, M. Kaya and M. Zahmakiran, *Appl. Catal., B*, 2016, **180**, 53–64.
16 A. Nasri, B. Jaleh, Z. Nezafat, M. Nasrollahzadeh, S. Azizian, H. W. Jang and M. Shokouhimehr, *Ceram. Int.*, 2021, **47**, 3565–3572.
17 T. Liu, Z. Zhang, L. Yan, Z. Zhang, Y. Zhang and Y. Yin, *Int. J. Hydrogen Energy*, 2021, **46**, 33098–33106.
18 J. Hao, Z. M. Cui, C. Y. Cao and W. Song, *Chem. Phys. Lett.*, 2016, **658**, 88–91.
19 D. Y. Zheng, R. Bai, M. Li, R. Wang and Y. Gu, *ACS Sustainable Chem. Eng.*, 2023, **11**, 10219–10224.
20 N. J. Costa, L. L. Vono, R. Wojcieszak, É. Teixiera Neto, K. Philippot and L. M. Rossi, *Dalton Trans.*, 2017, **46**, 14318–14324.
21 H. A. Elazab, S. Moussa, K. W. Brinkley, B. F. Gupton and M. S. El Shall, *Green Processes Synth.*, 2017, **6**, 413–424.
22 K. Liu, A. Wang, Y. Mao, Z. Jia, Y. Su and X. Wen, *Mol. Catal.*, 2023, **543**, 113130.
23 H. Veisi, S. Najafi and S. Hemmati, *Int. J. Biol. Macromol.*, 2018, **113**, 186–194.
24 T. Chen, Q. Chu, M. Li, G. Han and X. Li, *J. Nanobiotechnol.*, 2021, **19**, 1–13.

25 Q. Fang, J. Zhang, L. Bai, J. Duan, H. Xu, K. C. F. Leung and S. Xuan, *J. Hazard. Mater.*, 2019, **367**, 15–25.
26 H. Qu, L. Yang, J. Yu, L. Wang and H. Liu, *Ind. Eng. Chem. Res.*, 2018, **57**, 9448–9456.
27 J. Zhang, R. Cao, W. Song, L. Liu and J. Li, *J. Colloid Interface Sci.*, 2022, **607**, 1730–1740.
28 H. L. Cao, C. Liu, F. Y. Cai, X. X. Qiao, A. B. Dichiara, C. Tian and L. Jian, *Water Res.*, 2020, **179**, 115882.
29 L. Wen, D. Wang, J. Xi, F. Tian, P. Liu and Z. W. Bai, *J. Catal.*, 2022, **413**, 779–785.
30 R. Das, V. S. Sypu, H. K. Paumo, M. Bhaumik, V. Maharaj and A. Maity, *Appl. Catal., B*, 2019, **244**, 546–558.
31 A. Barzkar, A. Salimi Beni, S. Parang and F. Salahshour, *Sci. Rep.*, 2023, **13**, 19940.
32 F. Heidari, M. Hekmati and H. Veisi, *J. Colloid Interface Sci.*, 2017, **501**, 175–184.
33 W. Ye, X. Shi, J. Su, Y. Chen, J. Fu, X. Zhao, F. Zhou, C. Wang and D. Xue, *Appl. Catal., B*, 2014, **160**, 400–407.
34 L. Bai, W. Jiang, M. Sang, M. Liu, S. Xuan, S. Wang, K. C. F. Leung and X. Gong, *J. Mater. Chem. B*, 2019, **7**, 4568–4580.
35 G. Liu, Q. Xiong, Y. Xu, Q. Fang, K. C. F. Leung, M. Sang, S. Xuan and L. Hao, *Colloids Surf., A*, 2022, **633**, 127860.
36 Y. He, K. Niu, L. Luo, L. Li, C. Cong and D. Gao, *ACS Sustainable Chem. Eng.*, 2019, **7**, 20102–20106.
37 W. N. Wang, P. Pei, Z. Y. Chu, B. J. Chen, H. S. Qian, Z. B. Zha, W. Zhou, T. Liu, M. Shao and H. Wang, *Chem. Eng. J.*, 2020, **397**, 125488.
38 J. Song, C. Jiang, Z. Liu, Z. Yang, Z. Wang, Q. Jiang and P. Ruuskanen, *Colloids Surf., A*, 2023, **665**, 131215.
39 P. Pandey, S. Kunwar and J. Lee, *J. Alloys Compd.*, 2020, **813**, 152193.
40 J. Jin, S. Wu, J. Wang, Y. Xu, S. Xuan and Q. Fang, *Dalton Trans.*, 2023, **52**, 2335–2344.
41 W. Cheng, K. Tang, Y. Qi, J. Sheng and Z. Liu, *J. Mater. Chem.*, 2010, **20**, 1799–1805.
42 M. Naguib, M. Kurtoglu, V. Presser, J. Lu, J. Niu, M. Heon, L. Hultman, Y. Gogotsi and M. W. Barsoum, *Adv. Mater.*, 2011, **23**, 4248–4253.
43 Q. Xiong, Q. Fang, K. Xu, G. Liu, M. Sang, Y. Xu, L. Hao and S. Xuan, *Dalton Trans.*, 2021, **50**, 14235–14243.
44 P. A. Bazuła, P. M. Arnal, C. Galeano, B. Zibrowius, W. Schmidt and F. Schüth, *Microporous Mesoporous Mater.*, 2014, **200**, 317–325.
45 Z. Zhao, L. Yu, L. Zheng, T. Guo, Z. Lv, S. Song and H. Zheng, *J. Hazard. Mater.*, 2022, **435**, 128998.
46 H. Guo, R. Zheng, H. Jiang, Z. Xu and A. Xia, *Molecules*, 2019, **24**, 1730.
47 Q. Fang, J. Wang, S. Wu, K. C. F. Leung, Y. Xu and S. Xuan, *J. Hazard. Mater.*, 2023, **445**, 130616.
48 P. Zhang, M. Shi, M. Fan, P. Jiang and Y. Dong, *J. Chin. Chem. Soc.*, 2018, **65**, 681–686.
49 J. Chang, Q. Zhang, Y. Liu, Y. Shi and Z. Qin, *J. Mater. Sci.: Mater. Electron.*, 2018, **29**, 8258–8266.
50 L. Zhang, C. Xiao, Z. Li, J. Guo, G. Du, X. Cheng and Y. Jia, *Appl. Surf. Sci.*, 2023, **618**, 156595.
51 K. Xu, J. Wu, Q. Fang, L. Bai, J. Duan, J. Li, H. Xu, A. Hui, L. Hao and S. Xuan, *Chem. Eng. J.*, 2020, **398**, 125571.
52 Y. Zhong, Y. Gu, L. Yu, G. Cheng, X. Yang, M. Sun and B. He, *Colloids Surf., A*, 2018, **547**, 28–36.
53 L. Bai, Y. Ouyang, J. Song, Z. Xu, W. Liu, J. Hu, Y. Wang and F. Yuan, *Materials*, 2019, **12**, 1497.
54 H. Lin, S. Gao, C. Dai, Y. Chen and J. Shi, *J. Am. Chem. Soc.*, 2017, **139**, 16235–16247.
55 C. Fang, X. Jiang, X. Wang, J. Hu and R. Li, *Appl. Surf. Sci.*, 2023, **615**, 156138.
56 J. Audevard, A. Benyounes, R. Castro Contreras, H. Abou Oualid, M. Kacimi and P. Serp, *ChemCatChem*, 2022, **14**, e202101783.
57 S. Shabani and M. Dinari, *Int. J. Biol. Macromol.*, 2021, **193**, 1645–1652.
58 B. Lakshminarayana, K. A. Kumar, M. Selvaraj, G. Satyanarayana and S. Ch, *J. Environ. Chem. Eng.*, 2020, **8**, 103899.
59 L. Deng, Y. Zou and J. Jiang, *Dalton Trans.*, 2021, **50**, 17235–17240.
60 K. Saravanakumar, V. S. Priya, V. Balakumar, S. L. Prabavathi and V. Muthuraj, *Environ. Res.*, 2022, **212**, 113185.
61 S. Sepahvand and S. Farhadi, *RSC Adv.*, 2018, **8**, 10124–10140.
62 Y. Huang, Z. Ding, Y. Li, F. Xi and J. Liu, *Molecules*, 2023, **28**, 4573.
63 X. Shu, Y. Chang, H. Wen, X. Yao and Y. Wang, *RSC Adv.*, 2020, **10**, 14953–14957.
64 C. Zhao, G. M. Shi, F. N. Shi, X. L. Wang and S. T. Li, *Colloids Surf., A*, 2022, **642**, 128612.
65 G. Liu, H. Liu, H. Xu, L. Zhu, C. Su, C. Gu and L. Li, *Spectrochim. Acta, Part A*, 2020, **239**, 118544.
66 X. Liu and F. Liu, *Carbohydr. Polym.*, 2023, **310**, 120726.
67 Y. Ren, C. Hao, Q. Chang, N. Li, J. Yang and S. Hu, *Green Chem.*, 2021, **23**, 2938–2943.
68 G. Liu, H. Wang, C. Xu, Q. Fang, H. Wang, Y. Xu, M. Sang, S. Xuan and L. Hao, *J. Mater. Chem. B*, 2023, **11**, 10678–10691.
69 Y. Cheng, D. Wang, Y. Mei and F. Sun, *Compos. Commun.*, 2020, **22**, 100485.

